



The Gaseous Blowout of the 30 Doradus Starburst Region in the LMC

Suraj Poudel¹, April Horton¹, Jo Vazquez¹, Kathleen A. Barger¹, Frances H. Cashman^{2,3}, Andrew J. Fox^{4,5},
Nicolas Lehner⁶, Scott Lucchini⁷, Dhanesh Krishnarao⁸, N. M. McClure-Griffiths⁹, Elena D’Onghia¹⁰,
Jason Tumlinson², Ananya Goon Tuli⁶, Lauren Sdun¹, Stone Gebhart¹, Katherine Anthony^{1,11}, Bryce Cole¹,
Jacco Th. van Loon¹², Julia Roman-Duval², Yik Ki Ma⁹, Callum Lynn⁹, Min-Young Lee¹³, and Denis Leahy¹⁴

¹Department of Physics & Astronomy, Texas Christian University, Fort Worth, TX 76129, USA

²Space Telescope Science Institute, 3700 San Martin Drive, Baltimore, MD 21218, USA

³Department of Physics, Presbyterian College, Clinton, SC 29325, USA

⁴AURA for ESA, Space Telescope Science Institute, 3700 San Martin Drive, Baltimore, MD 21218, USA

⁵Department of Physics and Astronomy, Johns Hopkins University, 3400 N. Charles St., Baltimore, MD 21218, USA

⁶Department of Physics and Astronomy, University of Notre Dame, Notre Dame, IN 46556, USA

⁷Center for Astrophysics | Harvard & Smithsonian, 60 Garden Street, Cambridge, MA 02138, USA

⁸Department of Physics, Colorado College, Colorado Springs, CO 80903, USA

⁹Research School of Astronomy & Astrophysics, Australian National University, Canberra, ACT 2611, Australia

¹⁰Department of Astronomy, University of Wisconsin, Madison, WI 53706, USA

¹¹Department of Computing, Mathematics and Physics, Messiah University, Mechanicsburg, PA 17055, USA

¹²Lennard-Jones Laboratories, Keele University, ST5 5BG, UK

¹³Korea Astronomy and Space Science Institute 776 Daedeok-daero, Yuseong-gu, Daejeon 34055, Republic of Korea

¹⁴Department of Physics and Astronomy, University of Calgary, Calgary, AB T2N 1N4, Canada

Received 2024 July 25; revised 2025 March 3; accepted 2025 March 6; published 2025 May 8

Abstract

Widespread galactic winds emanate from the Large Magellanic Cloud (LMC), with the 30 Doradus starburst region generating the fastest and most concentrated gas flows. We report on the gas distribution, kinematics, and ionization conditions of the near-side outflow along eight down-the-barrel sightlines using UV absorption-line observations from the Hubble Space Telescope’s Ultraviolet Legacy Library of Young Stars as Essential Standards (ULLYSES) program for this region along with H I 21 cm observations from the Parkes Galactic All-Sky Survey (GASS) and Galactic Australian Square Kilometre Array Pathfinder (GASKAP) survey. We find that within $\Delta\theta \lesssim 1.7$ from the center of 30 Doradus, the wind reaches maximum speeds of $100\text{--}150\text{ km s}^{-1}$ from the LMC’s disk. The total integrated column densities of low ions (O I, Si II, and Fe II) in the blueshifted wind, up to $v_{\text{LSR}} = 150\text{ km s}^{-1}$, are highest near the center and decline radially outward. We estimate an outflow mass of $M_{\text{outflow, Si II}} \approx (5.7\text{--}8.6) \times 10^5 M_{\odot}$, outflow rate of $\dot{M}_{\text{outflow}} \gtrsim 0.02 M_{\odot} \text{ yr}^{-1}$, and mass loading factor of $\eta \gtrsim 0.10$ within $\Delta\theta \lesssim 0.52$ from the center of 30 Doradus. The observed ion ratios—together with photoionization modeling—reveal that this wind is roughly 40%–97% photoionized. The metallicities and dust depletion patterns of the high-velocity absorbers at $v_{\text{LSR}} \approx +120\text{ km s}^{-1}$ can be explained by either a foreground Milky Way (MW) halo cloud or an outflow from the LMC. For the high ions, Si IV and C IV are broader and kinematically offset from the low ions, suggesting turbulent mixing layers existing in the wind. Finally, our hydrodynamical simulations of the Magellanic Clouds and MW system suggest that the Magellanic Corona can protect the LMC winds from the ram pressure forces exerted by the MW’s halo.

Unified Astronomy Thesaurus concepts: Circumgalactic medium (1879); Galactic winds (572); Large Magellanic Cloud (903)

Materials only available in the online version of record: machine-readable table

1. Introduction

Galactic winds are high-speed outflows of gas and dust that emanate from galaxies at large scales. They are driven by a variety of processes, including the energy and momentum generated by supernovae, active galactic nuclei (AGN), stellar winds, and other sources of galactic feedback. The interplay between outflows associated with galactic winds and inflows represents a delicate balance that is a major part of the baryon cycle. Star formation feedback can induce large-scale gas circulation in the circumgalactic medium (CGM) and interstellar medium (ISM) that help to regulate the galaxy’s star formation

rate and chemical composition (S. Veilleux et al. 2005, B. D. Oppenheimer & R. Davé 2008).

Despite the importance of galactic winds, our understanding of their behavior and effects on both small (tens of parsec) and large (tens of kiloparsec) scales is limited. Galactic winds are diffuse and faint, and are therefore difficult to detect. Absorption-line studies are far more sensitive than imaging and emission-line studies to low-density material as they scale linearly with density, as opposed to the density squared, but are unable to map the wind’s properties. Further, degeneracies in the measurable properties of CGM material typically limit our ability to determine its origin, whether from an AGN, stellar feedback, a neighboring galaxy, halo-gas condensations, or the intergalactic medium. Accurately establishing the presence of outflows is challenging except at the disk and halo interface.

The Large Magellanic Cloud (LMC) is an ideal galaxy for studying the impact of stellar feedback due to its proximity at



Original content from this work may be used under the terms of the [Creative Commons Attribution 4.0 licence](https://creativecommons.org/licenses/by/4.0/). Any further distribution of this work must maintain attribution to the author(s) and the title of the work, journal citation and DOI.

Table 1
Target Properties

ID	Background Target	Stellar Type	l (deg)	b (deg)	$\Delta\theta_{30 \text{ Dor}}^a$ (deg)	$\Delta D_{30 \text{ Dor}}^a$ (kpc)	UV Observing ^b Modes
(1)	BAT99 105	O2 If*	279°46	−31°67	3.4×10^{-3}	2.9×10^{-3}	HST/STIS E140M+FUSE
(2)	Sk − 69°246	WN5/6h+WN6/7h	279°38	−31°66	6.5×10^{-2}	5.6×10^{-2}	HST/STIS E140M E230M+FUSE
(3)	Sk − 68°135	ON9.7Ia+	279°26	−31°77	1.9×10^{-1}	1.7×10^{-1}	HST/STIS E140M E230M+FUSE
(4)	BI 214	O6.5(n)(f)p	279°89	−32°04	5.2×10^{-1}	4.5×10^{-1}	HST/STIS E140M
(5)	Sk − 69°175	WN11h	279°55	−32°32	6.5×10^{-1}	5.7×10^{-1}	HST/STIS E140M E230M+FUSE
(6)	Sk − 68°112	O7.5(n)(f)p	278°99	−32°41	8.4×10^{-1}	7.3×10^{-1}	HST/STIS E140M
(7)	BI 173	O8II	279°66	−32°68	1.0	9.0×10^{-1}	HST/STIS E140M E230M+FUSE
(8)	Sk − 69°104	O6Ib(f)	279°92	−33°38	1.7	1.5	HST/STIS E140M E230M+FUSE

Notes.

^a These angular and projected distance offsets are from the center of 30 Doradus at $(l, b) = (279^\circ 46, -31^\circ 67)$ at an assumed distance of $d_\odot = 50$ kpc to our LMC target.

^b We assumed the following widths for the Gaussian-shaped line-spread function for the observing modes: $\text{FWHM}_{\text{res}} \approx 6.5 \text{ km s}^{-1}$ ($R \approx 45,800$) for STIS E140M, $\text{FWHM}_{\text{res}} \approx 10 \text{ km s}^{-1}$ ($R \approx 30,000$) for STIS E230M, and $\text{FWHM}_{\text{res}} \approx 20 \text{ km s}^{-1}$ ($R \approx 15,000$) for FUSE.

$d_\odot = 50$ kpc away (R. de Grijs et al. 2014 and references therein) and its face-on orientation at an inclination angle of $i \approx 23.4^\circ$ (Y. Choi et al. 2022). This galaxy shows no sign of AGN activity in X-ray emission (e.g., S. Kozłowski et al. 2012), which indicates that its galactic winds are mostly powered by its stars. Elevated stellar activity is observed extensively throughout the LMC’s disk, which encompasses 400 H II regions (e.g., R. D. Davies et al. 1976, E. W. Pellegrini et al. 2012) and more than 50 supernova remnants (SNRs; P. Maggi et al. 2016; D. A. Leahy 2017).

Several UV absorption-line studies have detected a large-scale outflow from the LMC, including N. Lehner & J. C. Howk (2007), K. A. Barger et al. (2016), Y. Zheng et al. (2024), and references therein. Additionally, the studies of L. Staveley-Smith et al. (2003) and D. A. Ciampa et al. (2021) have mapped this wind in 21 cm HI and H α emission, respectively. K. A. Barger et al. (2016) confirmed that these outflows are associated with a galactic wind due to their symmetry on both sides of the galaxy, and estimated that the winds have a mass of $M_{\text{wind}} \geq 10^7 M_\odot$. D. A. Ciampa et al. (2021) established that the 30 Doradus region of the LMC—the region with the most extreme stellar activity—is producing the fastest and most concentrated winds.

In this study, we investigate the properties of the winds produced by the 30 Doradus starburst using UV absorption- and H I 21 cm emission-line observations toward LMC disk stars. In Section 2, we describe these observations and their reduction. We outline our process for identifying the LMC’s wind in Section 3. In Section 4, we summarize our technique for flux normalization, fitting Voigt profiles to the absorption features, and handling overly saturated and blended lines. We analyze the gas distribution in Section 5, followed by gas kinematics in Section 6. We explore the ionization state of the wind using ion ratios and CLOUDY radiative transfer simulations in Section 7. In Section 8, we discuss the results from the high-resolution simulation of the LMC. We discuss our results and put them in context of previous studies in Section 9, and summarize our main conclusions in Section 10.

2. Observation and Data Reduction

We explore the galactic wind along eight sightlines within 1.7 of 30 Doradus (see Table 1 and Figure 1). We choose these

sightlines to lie preferentially to one side of 30 Doradus to avoid possible Magellanic tidal structures, such as the Magellanic Stream (E. D’Onghia & A. J. Fox 2016). Below, we discuss the observational details and data reduction steps for the UV absorption-line and radio emission-line data utilized in this work.

2.1. UV Absorption-line Data

All of our UV absorption-line observations are from the Hubble Space Telescope’s (HST’s) Ultraviolet Legacy Library of Young Stars as Essential Standards (ULLYSES; J. Roman-Duval et al. 2020) Director’s Discretionary Program. This science-ready spectroscopic library includes observations of high-mass stars in the LMC with typical signal-to-noise ratios (S/Ns) per resolution element for the stellar continuum of $20 \lesssim \text{S/N} \lesssim 30$. For our sample, we selected the background O stars from the Data Release 5 catalog as this was the release that was available at the time of our selection. Although we initially used that data release, we reran our analysis scripts on the observations from Data Release 6 once they became available, and present that analysis here. For this study, we only included the HST Space Telescope Imaging Spectrograph (STIS) observations for their higher spectroscopic resolution at a full width at half-maximum of $\text{FWHM}_{\text{STIS}} \approx 6.5\text{--}10 \text{ km s}^{-1}$ compared to the $\text{FWHM}_{\text{COS}} \approx 17 \text{ km s}^{-1}$ for the Cosmic Origin Spectrograph (COS). These sightlines were confined opposite to an H I overdensity filament known as Arm B (see Figure 1) to minimize potential contamination. D. L. Nidever et al. (2008) performed a Gaussian decomposition of the LAB H I survey ($\Delta\theta_{\text{LAB, res}} = 0.6^\circ$; P. M. W. Kalberla et al. 2005) and kinematically traced Arm B back to the region near 30 Doradus and then to the Magellanic Stream. With these criteria, there were a total of 10 O stars; however, two sightlines were removed from the final analysis due to having a noisy continuum, resulting in a total sample size of eight. Out of our eight background O stars, there are two Wolf-Rayet (WR) stars (see Table 1).

The STIS observations have the additional benefit of being less affected by atmospheric airglow that contaminates the O I $\lambda 1302$ and Si II $\lambda 1304$ lines due to its much smaller aperture. All of our targets were observed with the E140M diffraction grating centered at $\lambda_{\text{center}} = 1425 \text{ \AA}$, which covers a wavelength range of $1140 \lesssim \lambda \lesssim 1735 \text{ \AA}$. For five out of the

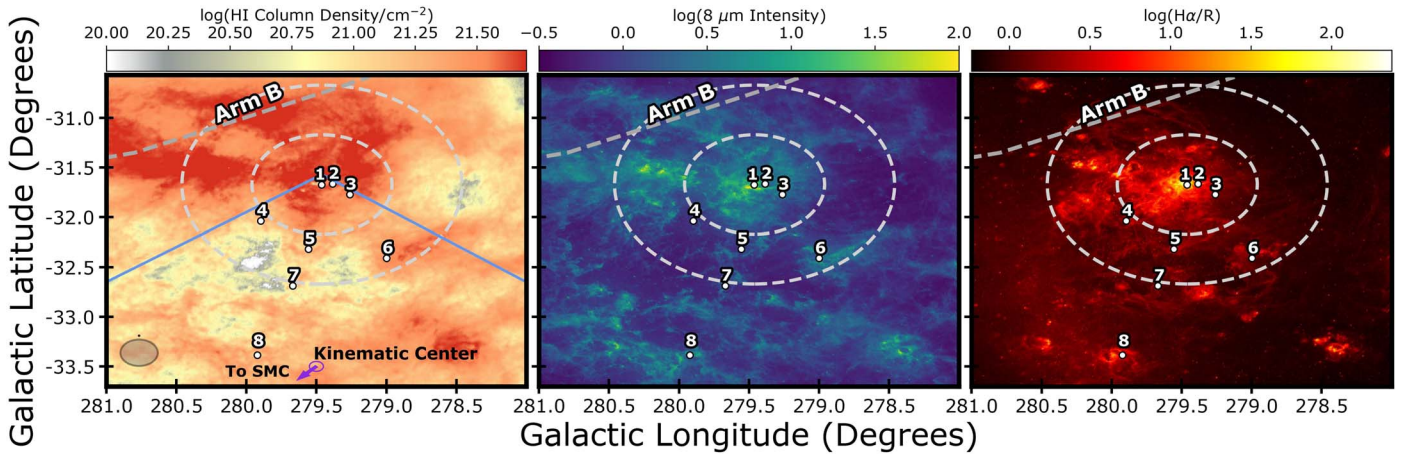


Figure 1. Left: integrated H I emission map of the Large Magellanic Cloud's (LMC's) disk over the range of $+185 \leq v_{\text{LSR}} \leq +335 \text{ km s}^{-1}$ using GASKAP observations. Middle: $8 \mu\text{m}$ emission using Spitzer observations. Right: $\text{H}\alpha$ emission from the Magellanic Cloud Emission-line Survey (MCELS; R. C. Smith & MCELS Team 1999). The positions of our eight stellar targets are marked with white points and have labels that match the indices listed in Table 1. The two dashed circles are centered at 30 Doradus and have radii of 0.5° and 1° . The small purple circle at the bottom of the H I map represents the kinematic H I center of the LMC, and the arrow indicates the direction of the Small Magellanic Cloud (SMC). The dashed gray diagonal line at the top left of the map tracks the position of a gaseous H I overdensity filament known as Arm B (S. Kim et al. 1998; L. Staveley-Smith et al. 2003). We choose background stellar targets that are confined within a downward angular cone centered at 30 Doradus (marked by the two solid lines) to avoid the H I overdensity filament. The gray circle positioned at the bottom left of the left-hand panel depicts the angular resolution of GASS at $\Delta\theta_{\text{GASS,res}} = 16'$, and the tiny black dot immediately above it represents the GASKAP angular resolution at $\Delta\theta_{\text{GASKAP,res}} = 30''$.

eight targets, the ULLYSES survey additionally observed them with the E230M grating, which covers a wavelength range of $1700 \lesssim \lambda \lesssim 3100 \text{ \AA}$. All UV observing modes are listed in Table 1.

The data reduction procedure for the ULLYSES data products is described in J. Roman-Duval et al. (2020) and at the survey's website.¹⁵ Here we provide a brief summary of their procedure. The STIS observations were run through the calibration pipeline (CalSTIS), which calibrated the flux and the wavelength and applied any wavelength shifts to align the spectra. Observations that were taken with the same instrument and diffraction grating were coadded. Observations taken with different instruments or diffraction gratings were abutted when the spectra did not overlap such that the wavelength arrays and dispersion are discontinuous at the transition point; overlapping spectra were truncated then abutted at a transition wavelength and have a spectral sampling that is discontinuous at that transition.

The ULLYSES archive additionally provides science-ready Far-Ultraviolet Spectroscopic Explorer (FUSE) spectral products that we incorporate when available, as they also cover the $\text{O I } \lambda 1039$ absorption features, which can be used when $\text{O I } \lambda 1302$ is saturated. Of our eight targets, five of them were also observed with FUSE in the far-UV, which has a kinematic resolution of $\text{FWHM}_{\text{FUSE}} \approx 20 \text{ km s}^{-1}$ and with typical S/Ns per resolution element for the stellar continuum of $\text{S/N} \approx 10$ (see Table 1).

2.2. Radio Emission Line

To investigate the neutral hydrogen gas phase in the LMC and its wind, we used H I 21 cm emission-line data from two surveys that offer different advantages in terms of sensitivity and resolution. We utilized the sensitive Galactic Australian Square Kilometre Array Pathfinder (GASKAP) survey (J. M. Dickey et al. 2013; N. M. Pingel et al. 2022) to explore

the relatively bright gas within the disk of the LMC. The GASKAP-HI Pilot Survey II data of the LMC that we used here have a sensitivity of $\log(N_{\text{HI}, 3\sigma} / \text{cm}^{-2}) = 20.0$ for typical clouds with $\text{FWHM} = 30 \text{ km s}^{-1}$, and a spatial resolution of $\Delta\theta_{\text{res}} = 30''$. The raw kinematic resolution of these data is $\Delta v_{\text{bin}} = 0.2 \text{ km s}^{-1}$; we binned the data cubes to $\Delta v_{\text{bin}} = 1 \text{ km s}^{-1}$ to smooth stochastic variations associated with noise. Further, we constrain the kinematic extent of the LMC's H I disk along our sightlines using this survey as it has a higher spatial resolution; the smaller beam of GASKAP translates to less blending of emission from gas surrounding our UV sightlines (i.e., beam smearing), which broadens the emission due to variations in gas motion.

Because GASKAP lacks the surface brightness sensitivity to detect the LMC's wind, we also employ data from the Parkes Galactic All-Sky Survey (GASS; P. M. W. Kalberla et al. 2010) to measure H I column densities for the wind. The GASS survey is 63 times more sensitive than GASKAP, at $\log(N_{\text{HI}, 3\sigma} / \text{cm}^{-2}) = 18.2$ for lines of $\text{FWHM} = 30 \text{ km s}^{-1}$, but has a much larger spatial resolution of $\Delta\theta_{\text{res}} = 16'$ (32 times larger than GASKAP; see left-hand panel of Figure 1).

3. Wind Identification

Because of the physical placement of the targets within the disk of the LMC, we are only sensitive to the nearside portion of the LMC's galactic wind, which is kinematically blueshifted. However, besides the LMC wind, numerous absorbers such as the Milky Way's (MW's) ISM, intermediate-velocity clouds (IVCs; $+30 \lesssim v_{\text{LSR}} \lesssim +90 \text{ km s}^{-1}$), high-velocity clouds (HVCs; $+90 \lesssim v_{\text{LSR}} \lesssim +175 \text{ km s}^{-1}$), and the LMC's ISM are found between the systemic velocities of the MW and LMC (N. Lehner & J. C. Howk 2007; J. Roman-Duval et al. 2019 and references therein). Additionally, there can also be circumstellar absorbers associated with the background stellar targets that are embedded in the LMC's disk, and also absorption features associated with coronal material in the MW's and LMC's halo (see D. Krishnarao et al. 2022 for a

¹⁵ <https://ullyses.stsci.edu>

recent discovery of the Magellanic Corona). In the sections below, we outline our method for identifying the LMC’s wind.

3.1. Checking the Stellar Environment

Our UV background targets for this study include O and WR stars that are luminous, hot, and massive. Their high luminosities translate into higher radiation pressures at the stellar surfaces, which can drive local stellar winds. The radiation and cosmic rays that emanate from their stellar surfaces ionize the surrounding circumstellar material, creating H II regions. The approaching side of these H II regions will be blueshifted relative to the star and can be kinematically confused with the LMC wind. For example, K. A. Barger et al. (2016) found that the expanding H II region surrounding the WR star HD33133—a star that lies in a relatively quiescent quadrant of the LMC—reaches out to about 100 km s^{-1} from the LMC’s systemic velocity in that direction. In active regions of star formation, such as the core of 30 Doradus, stellar contamination can be notably pronounced as the H II shells from either stellar winds or supernovae explosions can overlap (E. I. Doran et al. 2013; J. T. van Loon et al. 2013). As a consequence, certain absorption features detected in the spectra could potentially arise from the wind nebula enveloping the star rather than from the LMC’s galactic winds.

To distinguish the absorption components originating from the stellar nebula, we employed stellar catalogs, such as the one compiled by C. W. Danforth et al. (2002). This resource allowed us to investigate the circumstellar medium encompassing these background stars. Specifically, the work by C. W. Danforth et al. (2002) presented H α images of the regions surrounding four sightlines studied in this paper: Sk $- 68^\circ 135$, Sk $- 69^\circ 175$, Sk $- 69^\circ 246$, and BI 173. These images illuminated the morphology of warm ionized gas in the proximity of these stars. However, we found no morphological indications of wind nebulae encircling these stars. Additionally, we meticulously examined the locations of our sightlines using the Magellanic Cloud Emission Line Survey (MCELS) in the bright emissions of H α [6563], [S II] 6724, and [O III] 5007 from the interstellar gas (see right panel in Figure 1 for the H α image). We do not observe circumstellar structures in the gas surrounding most of our targets, with the exception of the sightlines toward BAT99 105 and Sk $- 69^\circ 104$. In the direction of these stellar targets, the H α emission is elevated and more structured (see the last panel in Figure 1). However, the spectra for these two stars do not contain features that are more distinct than those of the other stars, possibly suggesting that the LMC wind largely dominates the absorption associated with the circumstellar structures.

3.2. Conversion of Reference Frames

To assist in the identification and separation of the MW’s HVCs, LMC’s winds, and LMC’s ISM, we explore the UV spectra in both the kinematic local standard of rest (LSR) and the LMC standard of rest (LMCSR) frames. We utilize the LMCSR frame to identify wind components with respect to the center of the LMC. We converted the ULLYSES observations from the heliocentric reference frame to the kinematic LSR frame by taking into account the velocity offset of the Sun with respect to the LSR, which is approximately $\Delta v_{\text{LSR,offset}} \approx 20 \text{ km s}^{-1}$ toward the direction of (R.A., decl.) = (18 hr, $+30^\circ$).

We convert to the LMCSR reference frame by first estimating a central velocity offset. This offset is a function of the line-of-sight Galactic longitude (l) and Galactic latitude (b), and is calculated as follows from D. A. Ciampa et al. (2021):

$$\frac{\Delta v_{\text{LMCSR}}}{\text{km s}^{-1}} = 262.55 - 3.25(l - 280) + 3.66(b + 33). \quad (1)$$

We subtract this offset from the LSR velocity to convert into the LMCSR reference frame.

3.3. Separating the LMC’s Wind from the LMC’s Disk

The structure of the H I in the LMC’s disk varies a lot over kiloparsec scales (roughly 1° at the distance of this galaxy). We explored this using position–velocity plots that we generated with the GASKAP data set in which we sliced through the disk in both Galactic longitude and latitude (see Figure 2). Although we can characterize the global behavior of the disk by finding trends in the emission-weighted kinematic means and widths (i.e., first and second moments) in these slices, there is too much stochastic variation in the H I emission for these widths to be a good representation of the gas along the probed sightlines.

We therefore estimate the kinematic width of the H I disk using the closest GASKAP spectrum to each of our background stellar targets. We defined the kinematic boundaries of the disk to be where the H I emission is at least 3σ above the rms noise in the continuum, as illustrated in Figure 3. The widths obtained through this method generally match well with those of low ions. In a few cases, there were slight inconsistencies of about $5\text{--}10 \text{ km s}^{-1}$ when comparing the H I emission with the weak UV absorption metal lines, which may be attributed to the larger H I beam. Additionally, the H I emission probes gas through the entire thickness of the disk, while low ions probe only the gas foreground to the star. While we use this definition for consistency across all sightlines, we will also test different velocity cutoffs, particularly on the blue side of the disk, to determine if this causes any significant changes in the results we obtained about the wind (see Section 9, where we estimate the systematic error that might affect the outflow mass and outflow rate of the wind). For most other results, we do not find any significant changes. Moreover, the kinematic widths determined using neutral hydrogen may not accurately represent the characteristics of the disk for the high ions. The v_{LSR} velocities for the left (blueshifted) and right (redshifted) disk boundaries that we define for all eight sightlines we probe with UV observations are listed in Table 2. We shade the region that we associate with the LMC’s disk as gray in Figure 3 and in all of the plot stacks afterwards.

3.4. Separating the LMC’s Wind from the Milky Way’s HVCs

Numerous absorption features lie between the MW’s and LMC’s systemic velocities, corresponding to redshifted material with respect to the MW and blueshifted material with respect to the LMC. In general, the absorption at $v_{\text{LSR}} \lesssim +90 \text{ km s}^{-1}$ corresponds to the MW ISM and MW IVCs. However, the origin of the HVCs at $+90 \lesssim v_{\text{LSR}} \lesssim +175 \text{ km s}^{-1}$ remains unclear. Some studies conclude that high-velocity gas toward the LMC is associated with the MW halo (B. D. Savage & K. S. de Boer 1981; K. S. de Boer et al. 1990; P. Richter et al. 1999, 2015). Some of this high-velocity absorption is detected

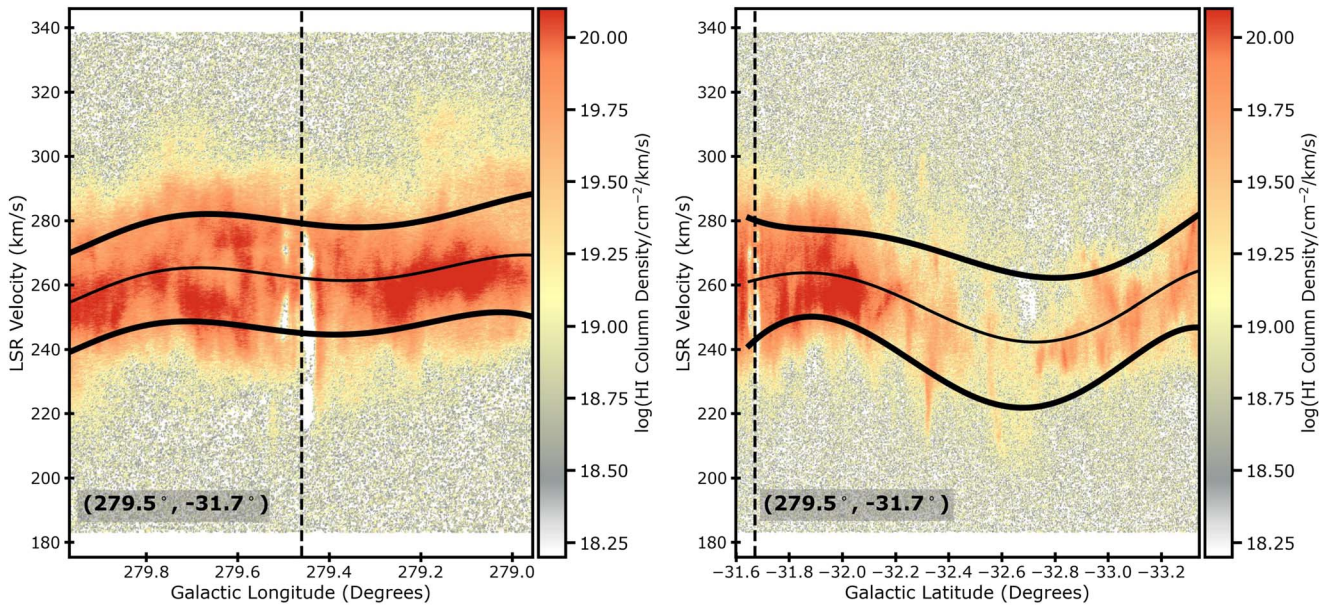


Figure 2. Position–velocity maps of the H I column density in the LMC’s disk using GASKAP observations for a positional slice through the total longitude and latitude space comprised by the eight sightlines. The left panel includes a horizontal slice at Galactic latitude (-31.7°), and the right panel a vertical slice at Galactic longitude (279.5°) of the sightlines. The vertical black dashed line represents the position of 30 Doradus. The thin solid black line is the kinematic center across the sliced region, and the thick solid black lines at the top and bottom mark the boundary of the LMC’s disk.

many degrees away from the Magellanic Clouds. Most of the MW’s HVCs are found to be within a distance of 10–20 kpc (N. Lehner et al. 2011, 2022). On the other hand, N. Lehner et al. (2009) conducted an investigation of the gas in front of the LMC using FUSE spectra of 139 early-type stars in the LMC as background targets and H I 21 cm emission data. Their examination of the HVCs spanning over the velocity range of $+90 \lesssim v_{\text{LSR}} \lesssim 175 \text{ km s}^{-1}$ suggested an LMC origin based on their distribution, metallicity, kinematics, and dust depletion patterns. In the D. A. Ciampa et al. (2021) H α emission-line study of the LMC’s galactic winds, they found that the 30 Doradus region produces winds with the greatest speeds, $v_{\text{LMCSR}} > -175 \text{ km s}^{-1}$, compared to the bulk material in the galaxy’s global winds at $v_{\text{LMCSR}} < -110 \text{ km s}^{-1}$. Winds at these extreme speeds exceed the escape velocity of the galaxy of $v_{\text{LMCSR,esc}} \approx 90 \text{ km s}^{-1}$ (K. A. Barger et al. 2016). D. A. Ciampa et al. (2021) further found that the H α morphology of the global wind is asymmetric such that the wind is more concentrated in the 30 Doradus quadrant of the galaxy. Given that absorption in the range $+90 \text{ km s}^{-1} \lesssim v_{\text{LSR}} \lesssim +175 \text{ km s}^{-1}$ has been the subject of debate regarding their origins, whether from the MW’s HVC or the LMC’s wind, we thoroughly analyze them to investigate their potential origins and properties in more detail in Sections 5, 6, and 7.

4. UV Absorption-line Analysis

We explore LMC outflow and coincidental inflow absorption features associated with the following spectral transitions that are covered by the HST/STIS observations: O I $\lambda 1302$, S II $\lambda \lambda 1250, 1253$, Fe II $\lambda 1608, 2249, 2260, 2344$, Al II $\lambda 1670$, Al III $\lambda \lambda 1854, 1862$, Si II $\lambda \lambda 1526, 1808$, Si IV $\lambda 1393, 1402$, and C IV $\lambda \lambda 1548, 1550$. Additionally, in some cases we also explore the weaker O I $\lambda 1039$ absorption features covered by FUSE because the O I $\lambda 1302$ is often saturated. We do not examine absorption for the C II $\lambda 1334$ transition because the MW’s C II $\lambda 1335$ absorption overwhelms any signatures of the LMC’s wind. We also exclude

the Si III $\lambda 1206$ line as it is in the wing of the MW’s Ly α signature where the S/N is too low to reliably use that transition.

4.1. Continuum Normalization

For each of the low-ion transitions that we explored, we created smaller spectral snippets that spanned $-1500 \lesssim v_{\text{LSR}} \lesssim +1500 \text{ km s}^{-1}$ for well-behaved continuum. We fit the stellar continuum using polynomials that have a typical order of $3 \leq n \leq 8$. These polynomial orders tend to be larger than those typically used for observations with quasi-stellar objects, as the background target of the stellar continuum of massive stars tends to be intricate as it is imprinted by stellar winds and rotation. These imprints tend to be more severe for the high-ion transitions. We established best-fit polynomial orders using goodness-of-fit tests by minimizing the reduced chi-squared (χ^2), and used the smallest order that resulted in a marginal change in the χ^2 . The spectral regions, which exhibited absorption features inconsistent with the stellar continuum, were excluded from the fit. As an example, the continuum fits for several key transitions toward the sightline Sk $-69^\circ 246$, along with the masked regions, are shown in Figure 4.

For the high-ion species C IV and Si IV, we used Legendre polynomials of degrees 1–8 to fit each continuum. This fitting was done within a velocity range of $500\text{--}1000 \text{ km s}^{-1}$ from the absorption line of interest. The choice of polynomial degree was determined by the complexity of the stellar continuum around the absorption lines. When the continuum was well behaved, we employed a low-degree Legendre polynomial, typically less than 5 (see N. Lehner et al. 2011 for details). The continuum for high ions in the Sk $-69^\circ 175$ sightline is too complex to reliably model, we therefore do not provide any measurements of Si IV and C IV toward that star.

4.2. Voigt Profile Fitting

For all the absorption features, we fit the spectral lines with Voigt line profiles using the VOIGTFIT Python software

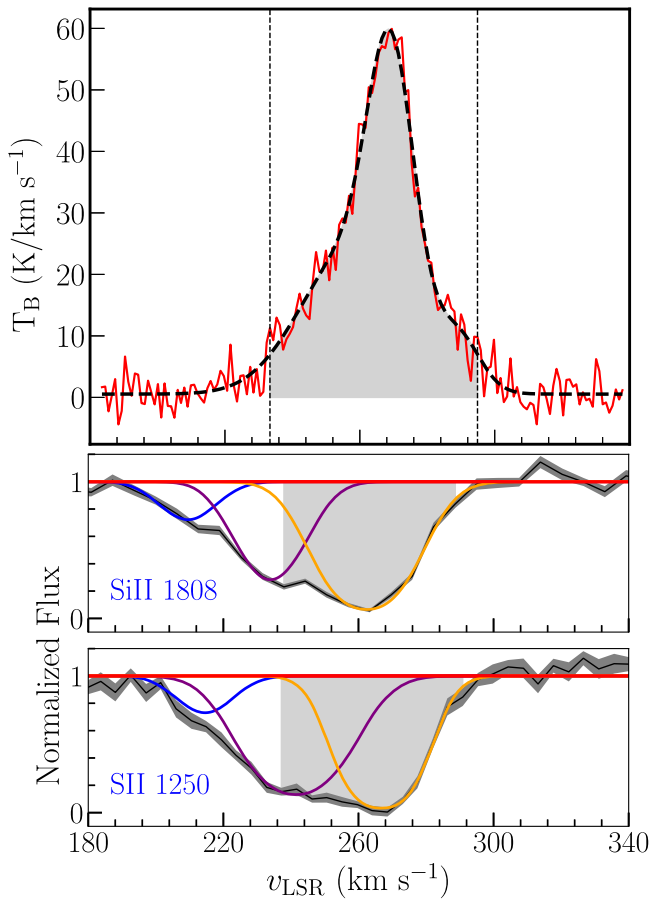


Figure 3. Determination of the kinematic width of the LMC’s disk by comparing the H I emission line with the UV absorption lines for the Sk – 69°246 sightline, which we have shaded in gray. In the upper panel, the red curve represents the H I emission data from GASKAP, and the black dashed curve is the corresponding multi-Gaussian fit to the data. The shaded region between the two vertical dashed lines represents the estimated LMC disk width, as described in Section 3.3. The lower panels display examples of weak UV absorption lines associated with this sightline. The horizontal line in red is drawn to show the position of the continuum, and the profiles in different colors represent the individual components from the Voigt profile fitting (see Section 4.2).

Table 2
LMC’s H I Disk Boundaries

ID	Sightline	Left Boundary ($v_{\text{LSR}}/\text{km s}^{-1}$)	Right Boundary ($v_{\text{LSR}}/\text{km s}^{-1}$)
(1)	BAT99 105	+243.1	+299.8
(2)	Sk – 69°246	+233.4	+294.9
(3)	Sk – 68°135	+233.4	+292.9
(4)	BI 214	238.2	+276.3
(5)	Sk – 69°175	+232.4	+285.0
(6)	Sk – 68°112	+238.2	+281.2
(7)	BI 173	+203.1	+249.0
(8)	Sk – 69°104	+225.5	+276.3

(version 3.14.1.1; J.-K. Krogager 2018). This software utilizes analytic approximation to the Voigt profile developed by T. Tepper-García (2006). We performed all of these fits using already continuum-normalized spectral segments for each ion transition. The VOIGTFIT program can fit various atomic lines with multiple components simultaneously and hold the Doppler

parameters (b), line centers (v), and column densities (N) fixed or allow them to freely vary. To determine column densities, the VOIGTFIT program uses atomic data (i.e., rest-frame wavelengths and oscillator strengths of transitions) from both the Vienna Atomic Line Data Base (or VALD; N. E. Piskunov et al. 1995) and F. H. Cashman et al. (2017). This line-fitting software determines the best fit through a nonlinear least-squares minimization. As the current version of VOIGTFIT does not have the functionality to use the tabulated line-spread function (LSF) for STIS (VOIGTFIT only supports the tabulated LSF for HST/COS), we accounted for the broadening associated with the detector by using a LSF with a Gaussian shape which has a FWHM that matches the spectral resolution of the instrument and mode of the observation. For example, we used a Gaussian profile with a $\text{FWHM}_{\text{res}} \approx 6.5 \text{ km s}^{-1}$ for the STIS E140M LSF that has a spectral resolution of $R \approx 45,800$; we list all of the FWHMs for the LSFs that we used for all observing modes in the footnotes of Table 1. The potential effects of using a Gaussian approximation to the LSF on the fit parameters, particularly column density and line width, have been explored in previous studies. A. J. Fox et al. (2020) specifically examined this for HST/COS observations of HVCs, and found no significant difference in the component parameters when using the tabulated LSF versus a Gaussian LSF. We have also tested this for the C IV and Si IV ions using a different software that utilizes the tabulated LSFs for the STIS E140M grating, and the differences in the $\log N$ values were less than 0.1 dex. Doppler b -values were also consistent within $<0.5\sigma$.

For the low ions, when multiple transitions of the same ion were available we fitted them independently. We prioritized lines based on their S/N and the degree of saturation, using the weaker lines (with lower oscillator strengths) when possible to avoid saturation effects. The stronger transitions (with higher oscillator strengths) are generally chosen to analyze the weak components in the wind, and the lines with weaker transitions are better for the strong components in the disk that often saturate. For example, we used the Si II $\lambda 1808$ transition for very strong components in the slow-moving part of the wind and in the LMC disk; however, we often used the Si II $\lambda 1526$ transition for the fast-moving wind components as they are often too weak to be detected in Si II $\lambda 1808$. Occasionally, we also compare the 3σ upper limit in the column density for a nondetection of the Si II $\lambda 1808$ line with the column density measured from Si II $\lambda 1526$. This comparison was helpful to check for unresolved saturation of the stronger Si II $\lambda 1526$ line. Similarly, for Fe II, we utilized the stronger Fe II $\lambda 1608$ and Fe II $\lambda 2344$ lines and the weaker Fe II $\lambda 2249$ and Fe II $\lambda 2260$ lines. We used both the S II $\lambda 1250$ and S II $\lambda 1253$ transitions to measure the S II column density.

For neutral oxygen, we constrained its column density using O I $\lambda 1302$ from STIS for most of our sightlines. However, for the Sk – 69°175 and BI 173 sightlines, we additionally used the O I $\lambda 1039$ line that is available through FUSE observations. For these two sightlines, this transition did not suffer from obvious airglow emission contamination. Although H₂ absorption is littered across the continuum for this transition, the LMC’s ISM and outflows were not significantly impacted. However, H₂ contamination litters the other parts of this spectral segment, impacting our continuum fit and adding uncertainty in our normalization. We accounted for the uncertainty in continuum placement by estimating the column

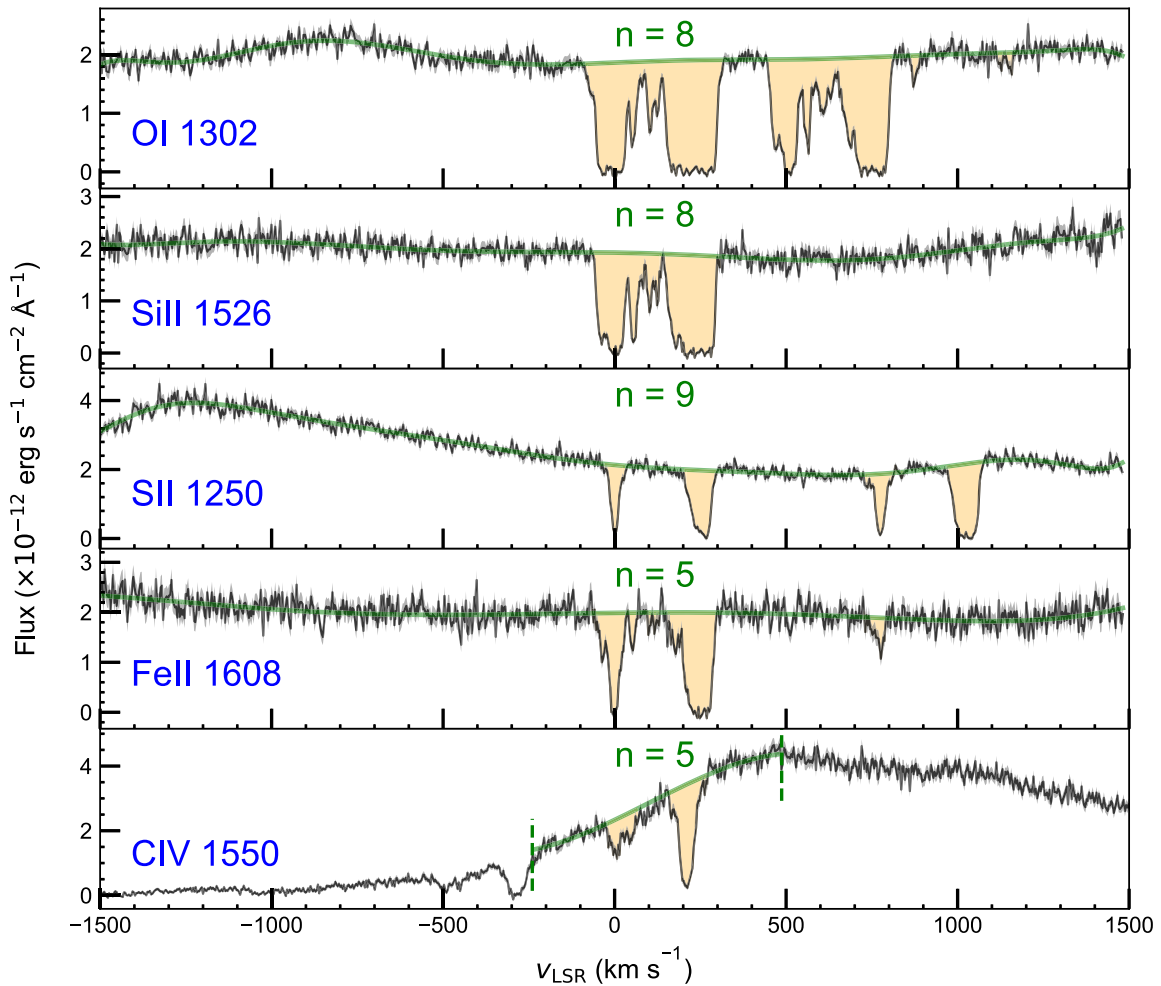


Figure 4. Nonnormalized spectra and associated continuum fits for a few key transitions observed toward the Sk – 69°246 background stellar target. In each panel, the data in black represents the observed flux, with the gray envelope indicating its uncertainty. The green lines mark the continuum fit. The absorption features shaded in yellow represent data excluded during the continuum-fitting process. The order of the polynomial fit “ n ” is provided in each panel. For C IV, only a small portion of the spectrum was used (see the region bounded by two vertical dashed lines in green) to fit the continuum due to the complexity of the stellar continuum.

densities based on the highest plausible continuum positions, and propagated the corresponding errors. For the Sk – 69°175 sightline, we identified absorption from the MW molecular line 4–0 R(2) $\text{H}_2\lambda 1051.5$ at $v_{\text{LSR}} \approx +320 \text{ km s}^{-1}$. However, since we were not interested in this velocity region, we masked the molecular hydrogen absorption components at this velocity when performing the Voigt profile fitting. The LMC component of the 5–0 R(2) $\text{H}_2\lambda 1038.7$ line may be contaminated with the O I $\lambda 1039$ absorption at $v_{\text{LSR}} \approx +120 \text{ km s}^{-1}$. To estimate the potential contribution to the O I HVC profile from this molecular line, we examined the absorption of the 4–0 R(2) $\text{H}_2\lambda 1051.5$ transition. This line was chosen because it is free from contamination by other lines and the stellar continuum near this region is clean. Moreover, the strengths of both of these transitions are comparable. We found that the contribution from the molecular hydrogen line was insignificant. While we generally allowed the velocity centroids for each ion to vary freely, there were some instances where we opted to fix them. In cases of saturation and blending (which is generally the case in the disk region), we fixed the velocity centroids for all blended or saturated lines to match lines produced by elements in similar ionization states that had the least blending and saturation.

In the case of high ions, we fitted the C IV and Si IV lines independently. However, the C IV doublets were fitted simultaneously, as were the doublets of Si IV. Moreover, we allowed for all of their fit parameters to typically vary freely. We list the Voigt profile fitting results used for our analysis for both the low and high ions for sightline Sk – 69°246 in Table 3. We list our fit results for all sightlines explored and analyzed in this study in the full machine-readable version of Table 3. While Table 3 lists the column densities and uncertainties produced by VOIGTFIT, we treat them as a lower limit in our analysis for cases of saturation. Such components are provided with a footnote (“a” for a component which might be saturated and “b” for a component which is saturated) in Table 3. In situations where a line is not detected, we provide a 3σ upper limit on the column density. We graphically illustrate the fits for each component along sightline Sk – 69°246 in Figures 3 and 5 and in Appendix A for all other sightlines.

We also rely on the apparent optical depth (AOD) method (B. D. Savage & K. R. Sembach 1991) to obtain total column densities within set velocity ranges that we use to explore trends across all sightlines (for example, see Section 5.1). This method involves converting the observed flux ($F(v)$) into an

Table 3
Results of Voigt Profile Fitting Analysis

Ion	v_{LSR} (km s ⁻¹)	v_{LMCSR} (km s ⁻¹) Sk - 69°246	$\log(N_k/\text{cm}^{-2})$	b (km s ⁻¹)
O I	+103.7 ± 0.6	-165.7	13.94 ± 0.03	7.7 ± 0.9
	+124.5 ± 0.9	-144.9	13.67 ± 0.06	6.7 ± 1.5
Si II	+102.2 ± 0.9	-167.2	13.37 ± 0.05	6.9 ± 1.3
	+123.6 ± 0.9	-145.8	13.30 ± 0.06	7.9 ± 1.6
	+177.6 ± 0.0 ^a	-91.8	14.17 ± 0.02	18.5 ± 1.0
Fe II	+209.5 ± 0.0	-59.9	14.82 ± 0.09	9.4 ± 2.7
	+103.1 ± 0.6	-167.9	13.03 ± 0.04	5.4 ± 1.4
	+123.0 ± 0.6	-146.9	12.93 ± 0.04	4.8 ± 1.7
	+175.7 ± 0.9	-93.7	13.83 ± 0.02	19.6 ± 1.1
	+206.5 ± 0.0	-62.9	13.78 ± 0.04	7.8 ± 1.0
S II	+102.2	-167.2	<13.76	...
	+123.6	-145.8	<13.60	...
	+177.6	-91.8	<13.64	...
	+214.5 ± 0.0	-54.9	14.56 ± 0.18	10.4 ± 3.1
Al II	+241.5 ± 3.9 ^a	-27.9	15.55 ± 0.12	16.7 ± 4.1
	+95.4 ± 1.8	-174.0	12.11 ± 0.13	8.3 ± 2.9
	+117.0 ± 1.8	-152.4	12.31 ± 0.09	10.7 ± 2.7
	+168.4 ± 4.2 ^a	-101.0	12.74 ± 0.15	16.7 ± 3.6
	+206.5 ± 0.0 ^b	-62.9	13.03 ± 0.11	19.5 ± 9.9
	+235.4 ± 0.0 ^b	-34.0	14.76 ± 0.36	15.7 ± 0.8
	+103.8 ± 1.2	-165.6	11.65 ± 0.24	5.5 ± 3.2
Al III	+124.3 ± 2.2	-145.1	11.79 ± 0.19	6.8 ± 1.5
	+177.6 ± 0.0	-91.8	11.51 ± 0.39	10.5 ± 2.2
	+206.5 ± 0.0 ^a	-62.9	13.31 ± 0.02	14.5 ± 3.1
	+235.4 ± 0.0	-34.0	12.96 ± 0.02	15.4 ± 2.7
C IV	+100.2 ± 0.0	-169.2	13.23 ± 0.07	28.2 ± 6.1
	+210.6 ± 0.3 ^b	-58.8	14.37 ± 0.01	22.5 ± 0.5
Si IV	+98.1 ± 3.0	-171.3	12.34 ± 0.01	14.4 ± 4.3
	+212.9 ± 0.3 ^b	-56.5	14.06 ± 0.01	22.6 ± 0.4

Notes. A summary of the Voigt profile fitting outcomes for +90 km s⁻¹ $\lesssim v_{\text{LSR}} \lesssim$ LMC's disk boundary across various ion species along sightline Sk - 69°246; we list the outcomes for all of our sightlines in the machine-readable version. We exclude the results for the components which are saturated and blended together as they may not represent the correct values. While the table lists the errors in column densities produced by VOIGTFIT, we treat them as a lower limit in cases of saturation, and such components are marked with a corresponding footnote. Since the Voigt profile fitting may not always provide a robust estimate of a lower limit on column density, we report only those values which are also consistent with the values obtained from the AOD method (for the components represented by the footnotes “a” and “b”). For these saturated lines, although we provide the b -values, we stress they are also less certain. In situations where a line is not detected, we provide a 3σ upper limit on the column density. In some cases, when we need to fix the velocity centroids, the errors for those particular components are set to 0.0 km s⁻¹. The errors in v_{LMCSR} are not listed in the table, as they are the same as the errors in v_{LSR} .

^a These components could potentially be saturated.

^b These components are saturated.

^c This component is affected by molecular absorption.

(This table is available in its entirety in machine-readable form in the [online article](#).)

apparent column density profile ($N_a = \int N_a(v) dv$):

$$\frac{N_a}{\text{cm}^{-2}} = \frac{3.768 \times 10^{14}}{f\lambda_o} \int \tau_a(v) \frac{\text{cm}^{-2}}{\text{km s}^{-1}} dv, \quad (2)$$

where λ_o is the rest wavelength of the transition in angstrom, and f is the corresponding oscillator strength. The optical depth

(τ) is related to the observed flux and continuum flux ($F_c(v)$) by

$$\tau_a(v) = \ln \left(\frac{F_c(v)}{F(v)} \right). \quad (3)$$

For lines with clear saturation (when the flux reaches zero), we adopt the AOD column densities as lower limits. We additionally compare the apparent column densities for different transitions of the same ion to check and correct for the unresolved saturation using the methods described in E. B. Jenkins (1996) and B. D. Savage & K. R. Sembach (1991). For unsaturated lines, the AOD column densities obtained from both the strong and weak transitions should be similar. Voigt profile fitting may not always provide a robust estimate of a lower limit on column density as it depends on the modeled b -value. Therefore, for the saturated components, we report only those values from the profile fits which are also consistent with the values obtained from the AOD method (see the components with footnotes “a” and “b” in Table 3).

5. Gas Distribution

To investigate the origin of the gas absorption toward 30 Doradus, we explore the kinematic and radial distribution of the gas using our eight stellar sightlines.

5.1. Radial Distribution of the Gas

We analyze the distribution of the gas absorption as a function of the angular offset from the center of 30 Doradus. For this, we calculated the total column densities for various atomic species in different velocity regions. First, we estimate the integrated column densities for Fe II, Si II, and O I for velocities that range from $v_{\text{LSR}} = +150 \text{ km s}^{-1}$ to the kinematic boundary of the LMC's galactic disk (see Table 4). We prefer the AOD method to adding individual components from the Voigt profile fitting to determine these column densities as we want to compare the sightlines over consistent velocity binning. Second, the kinematically neighboring components to the LMC disk boundary in the closest sightlines to 30 Doradus are mostly saturated, especially for O I. In cases of saturation, we treat the column densities as lower limits. We find that the integrated column densities of the blueshifted absorbers relative to the LMC's disk with $v_{\text{LSR}} > +150 \text{ km s}^{-1}$ decrease linearly as the angular offset from center of the 30 Doradus starburst region increases (see Figure 6). This characteristic holds for all three of the aforementioned atomic species. However, the most notable trend is observed in the Fe II column density distribution, which experiences less saturation compared to Si II and O I.

To test the robustness of the declining column densities with angular offsets, we perform a Kendall's tau test, which provides a reliable assessment of the monotonic association between two variables. Specifically, we implement a censored Kendall's tau analysis to account for lower limits in column density by treating censored values as greater than or equal to their observed limits. The Kendall rank correlation coefficient τ and the significance level of the correlation p for all the three ions are listed in Table 5. We adopt a p -value threshold of 0.05 to compare the level of significance. We get a large negative value of $\tau = -0.64$ with a value of $p = 0.03$, signifying a negative correlation between the Fe II column density and the angular offset from 30 Doradus. Although there is a negative

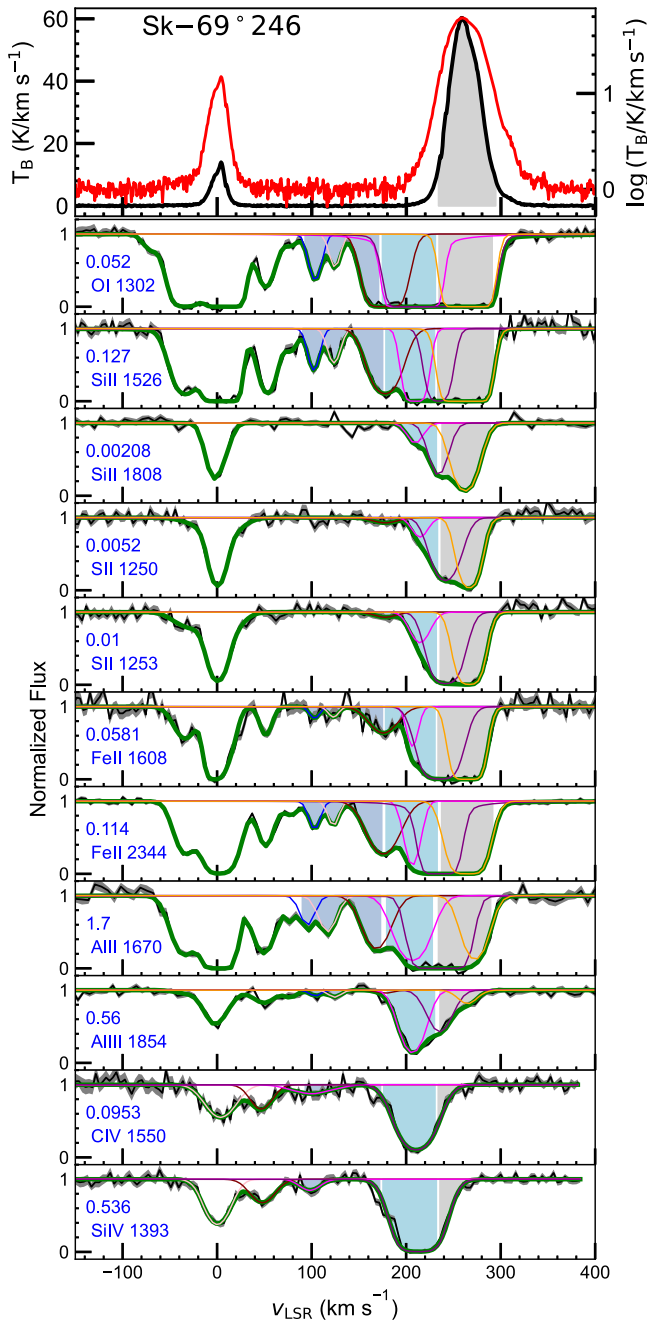


Figure 5. Upper panel: H I 21 cm emission-line data using GASS (P. M. W. Kalberla et al. 2010) for the Sk - 69°246 sightline (shown in black). The spectrum is also presented in a logarithmic scale (shown in red) to facilitate the visual magnification of possible weaker emission lines outside the disk. The shaded region marks the boundaries for the LMC’s H I disk (see Section 3.3 for details). Lower panels: Voigt profile fits to various metal absorption lines. The oscillator strength values for the corresponding transitions are provided in each panel. The normalized flux is depicted as a black curve, and the 1σ error is represented by the gray envelope around the normalized flux. The multicolored lines correspond to Voigt profile fits for individual components, while the green line represents the total coadded fit for all these components. As in the upper panel, the gray shaded region indicates LMC disk absorption. The different shades of blue correspond to the HVC ($+90 \text{ km s}^{-1} \lesssim v_{\text{LSR}} \lesssim +175 \text{ km s}^{-1}$) and the LMC wind ($+175 \text{ km s}^{-1} \lesssim v_{\text{LSR}} \lesssim \text{LMC's disk boundary}$). Similar plot stacks for the sightlines explored in this study are included in Appendix A.

correlation between the column density and the angular offset from 30 Doradus for Si II and O I, this correlation is not quite significant and is likely attributed to the elevated level of

saturation in the sightlines closest to this starburst region (see Figure 5 and Appendix A plot stacks). The closer the sightlines are to 30 Doradus, the larger is the radial velocity range in which the profile goes all the way to zero flux. Accounting for the saturation, the radial decrease of the column densities with projected distance from 30 Doradus would be stronger than suggested by the slopes in Figure 6.

We tested how varying the kinematic boundary affected how the column densities vary with increased projection distance from 30 Doradus. When we expanded the integration range by a small amount of $10\text{--}20 \text{ km s}^{-1}$, this did not have any significant change in the trend we obtained earlier. This is because there is a minimal contribution to the total integrated column densities from the components that lie between $+130 \leq v_{\text{LSR}} \leq +150 \text{ km s}^{-1}$. If we increased this integration range by 50 km s^{-1} to $v_{\text{LSR}} = +100 \text{ km s}^{-1}$, we still observe a radial decrease in the column densities, though including the absorbers in this region would soften the decline (see Figure 7). Indeed, examining the total column density distribution spanning the region $+100 \leq v_{\text{LSR}} \leq +150 \text{ km s}^{-1}$, we do not observe any specific trend in the data (see first panel in Figure 8). Moreover, we find no specific pattern in the integrated column density with respect to angular distance both in the velocity range of $v_{\text{LSR}} = +50$ to $+100 \text{ km s}^{-1}$ (see middle panel in Figure 8) and in $v_{\text{LSR}} = +50$ to $+150 \text{ km s}^{-1}$ (see third panel in Figure 8). This suggests that the absorption at the $v_{\text{LSR}} \gtrsim +150 \text{ km s}^{-1}$ is more likely associated with the LMC wind originating from 30 Doradus. The absorption at $v_{\text{LSR}} = +100$ to $+150 \text{ km s}^{-1}$ may be associated both with the MW HVCs and the LMC wind.

5.2. Kinematic Distribution of the Gas

We analyze the variations in component column densities derived from Voigt profile fitting for Fe II with respect to v_{LSR} in the entire velocity spectrum. We choose Fe II due to the availability of multiple transitions (Fe II λ 1608, 2249, 2260, 2344). The components associated with these transitions exhibit fewer issues with blending and saturation when compared to other ions, which enabled us to identify and characterize the largest number of components.

Our examination reveals a pattern in the column densities and velocities for absorbers within 0.52 from the center of 30 Doradus (see left panel of Figure 9). As we kinematically progress from the LMC’s disk region toward the MW, the column densities steadily decrease, reaching a minimum at approximately $v_{\text{LSR}} \approx +100 \text{ km s}^{-1}$ before starting to rise again as we approach the MW. For the offset = 0.52 curve, there appears to be a local minimum at $v_{\text{LSR}} \approx +200 \text{ km s}^{-1}$, which seems consistent with the column densities observed near $v_{\text{LSR}} \approx +100 \text{ km s}^{-1}$. However, the component at $v_{\text{LSR}} \approx +200 \text{ km s}^{-1}$ is less reliable due to its very narrow line width of 2.8 km s^{-1} and a larger error in column density of 0.21 dex. Additionally, this component is not observed in other ions along this sightline, suggesting it may not be a robust feature. Therefore, we consider the more significant minimum to be around $v_{\text{LSR}} \approx +100 \text{ km s}^{-1}$ for most of these first four sightlines, indicating a likely transition velocity. While some of the Fe II components in the LMC disk and the MW disk are potentially saturated, this does not affect the region where the column density is reaching toward the minimum value.

This trend is not obvious for the four farthest sightlines located from the center (see right panel of Figure 9). For the

Table 4
The Total AOD Column Densities Integrated between $v_{\text{LSR}} = +150 \text{ km s}^{-1}$ to the Left Boundary of the LMC’s H I Disk (see Table 2)

Sightline	Angular Offset (deg)	$\log N_{\text{FeII}}$	$\log N_{\text{SiII}}$	$\log N_{\text{OI}}$
BAT99 105	0.003	>14.80	>14.73	>15.24
Sk – 69°246	0.06	>14.50	15.28 ± 0.01	>15.16
Sk – 68°135	0.20	14.20 ± 0.04	15.30 ± 0.01	>15.12
BI 214	0.52	14.47 ± 0.03	>14.79	>15.30
Sk – 69°175	0.65	14.21 ± 0.05	14.42 ± 0.09	15.32 ± 0.02
Sk – 68°112	0.84	14.01 ± 0.06	>14.34	>14.82
BI 173	1.03	14.34 ± 0.19	>14.44	>15.02
Sk – 69°104	1.76	13.67 ± 0.01	14.15 ± 0.06	>14.55

outer sightlines, one can speculate the minimum column density may shift to $v_{\text{LSR}} \approx +150 \text{ km s}^{-1}$, as most of them show a local minima in the column density close to that velocity. We conducted a similar analysis for the high ions C IV and Si IV (see Figure 10), and find no distinct minimum in their column densities, though two sightlines near 30 Doradus exhibit minimum column density at around $v_{\text{LSR}} \approx +100 \text{ km s}^{-1}$.

If the lighter clouds ejected from a galaxy are more easily accelerated by momentum-driven forces, they should reach higher velocities. Additionally, if faster clouds traveling through an ambient medium disperse more rapidly due to stronger ram pressure effects, then we would expect higher-velocity material to be more diffuse. Under these assumptions, the observed trend—where the material moving at higher velocities relative to the LMC’s disk exhibits lower column densities—suggests that higher-speed gas is more diffuse. This pattern aligns with the inverse relationship between cloud speed (v_c) and column density ($v_c \propto \frac{1}{\sqrt{N}}$) observed in galactic winds (e.g., T. M. Heckman 2002; see also Appendix B). Within this framework, we interpret the velocity at which the column density reaches a minimum as the maximum speed at which detectable diffuse gas can escape the LMC’s gravitational pull. Beyond this minimum, the subsequent rise in column densities at even higher velocities may indicate a transition to material associated with the MW’s HVCs.

Under the assumption described above, the lack of a clear trend for the outer four sightlines (see right panel of Figure 9) may result from contamination of the LMC wind by the MW’s HVC as well as the LMC’s CGM in the velocity range of $v_{\text{LSR}} = +100 \text{ km s}^{-1}$ to $v_{\text{LSR}} = +150 \text{ km s}^{-1}$. A recent study by S. Mishra et al. (2024) detected the LMC’s CGM in several low-ionization species, including Fe II, out to an impact parameter of 17 kpc. While their column densities for Fe II are generally similar to the values we obtained for the wind components, the population of Doppler b -values they observed differs significantly from our results. However, we cannot entirely rule out the possibility that the LMC wind may also be contaminated by the LMC’s CGM. For the high ions, we believe that the LMC wind may be polluted by the LMC’s coronal gas (D. Krishnarao et al. 2022) at this high velocity, resulting in an absence of the trend of column density versus velocity obtained for the low ions. As the most active star-forming region in the LMC, 30 Doradus is expected to drive high-speed winds. D. A. Ciampa et al. (2021) have found evidence of similar-velocity outflowing gas from this region, reaching a maximum of 175 km s^{-1} relative to the LMC disk (or $v_{\text{LSR}} \approx 100 \text{ km s}^{-1}$) from H α emission-line observations.

A recent study by Y. Zheng et al. (2024) only considered the absorption at $v_{\text{helio}} > +175 \text{ km s}^{-1}$, assuming that material at

greater speeds relative to the LMC is less likely to be associated with the galaxy’s outflows. Their interpretation was based on the results from P. Richter et al. (2015), which reported an HVC associated with the MW at $v_{\text{LSR}} \approx +115 \text{ km s}^{-1}$. However, the sightline from P. Richter et al. (2015) was several degrees away from 30 Doradus and even outside the $\log(N_{\text{HI}}/\text{cm}^{-2}) \approx 18.5$ contour for the LMC’s disk.

Our primary focus in this study is the LMC’s outflows, which are blueshifted in absorption compared to the systemic velocity of the LMC using stars embedded within that galaxy’s disk. Using the same procedure for defining the kinematic bounds of the LMC’s gaseous disk that we used to identify outflowing material from this galaxy, we additionally find redshifted material that is presumably flowing toward it. Specifically, for three sightlines—Sk – 68°135, BI 214, and Sk – 68°112—we observe redshifted absorption in the low ions beyond the disk that is consistent with the weaker H I components from the GASS data. J. C. Howk et al. (2002) also reported a possible inflow toward a sightline, based on redshifted O VI, just within $\sim 0.2^\circ$ of Sk – 68°112. We have shaded the redshifted absorption associated with these sightlines in red in Figure 21 in Appendix A. This redshifted absorption might represent gas that is inflowing into the LMC that could be recycling back from the outflows.

6. Kinematics

The Doppler b -parameter characterizes the velocity spread of an absorption line. The b -values obtained through Voigt profile fitting represent the combined effects of both the thermal and nonthermal broadening in an absorption line. By comparing the b -values for different ions and for various sightlines, we can gain insight into the mechanisms that are responsible for the broadening of the absorption lines. Additionally, comparing the velocity centroids across different sightlines and various ions within the same sightline can offer crucial information about the potential origin of the gas and the distinct gas phases. We investigate these aspects throughout the velocity spectrum, extending from the MW to the LMC. Nevertheless, our main emphasis is on the region associated with the LMC wind.

6.1. Doppler b -parameter Distributions

We compare the magnitude of b -values across the entire velocity range from the MW to the LMC using Fe II (see details in Appendix C). The average b -value and the standard deviation from the mean for the LMC wind region ($+150 \lesssim v_{\text{LSR}} < +210 \text{ km s}^{-1}$) is found to be $\langle b \rangle_{\text{Fe II}} = 11.6 \pm 7.7 \text{ km s}^{-1}$ (see Table 6). These values for $+100 \lesssim v_{\text{LSR}} < +150 \text{ km s}^{-1}$ are $\langle b \rangle_{\text{Fe II}} = 8.3 \pm 3.4 \text{ km s}^{-1}$. We do not find any

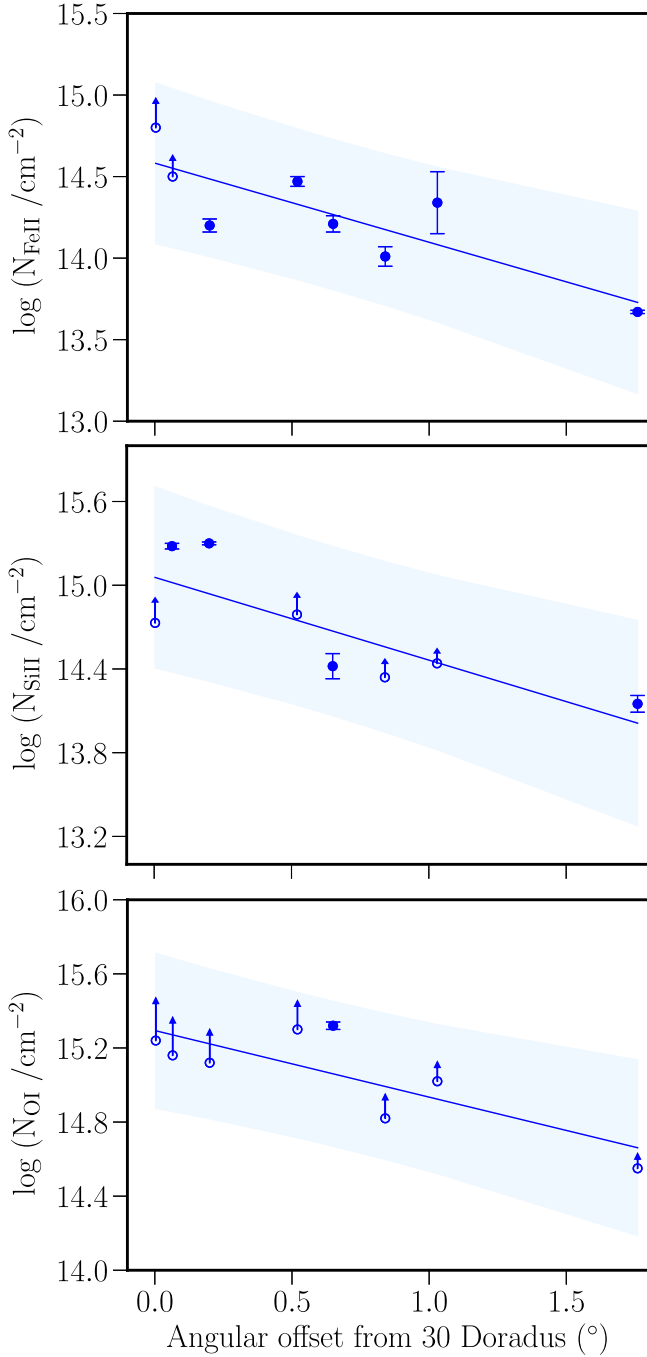


Figure 6. Variations in integrated column densities of Fe II, Si II, and O I as a function of angular separation from 30 Doradus in a velocity range of $+150 \text{ km s}^{-1} < v_{\text{LSR}} < \text{LMC's disk boundary}$, where the disk boundaries are defined in Table 2. The solid lines represent linear regression fits applied to the observed data points depicted by the circles. The open circles are presented without the error bars as these values are saturated. The upward-directed arrows represent the extent of saturation, with larger arrows signifying a higher level of saturation. The shaded region in blue shows the uncertainty in the fit.

significant differences in the average b -values between any of these regions. Moreover, we also do not observe any specific trend in the magnitude of b -values with respect to the angular distance from 30 Doradus.

We also estimate the average b -values and the standard deviations from the mean for the high ions to be $\langle b \rangle_{\text{C IV}} = 24.9 \pm 15.2 \text{ km s}^{-1}$ and $\langle b \rangle_{\text{Si IV}} = 18.4 \pm 11.9 \text{ km s}^{-1}$ for the

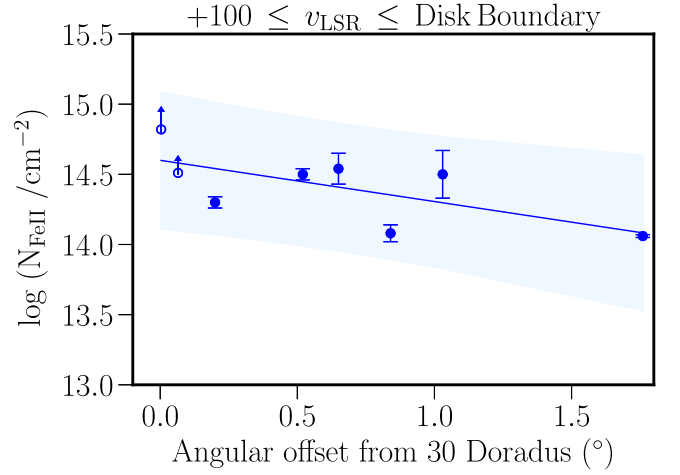


Figure 7. Similar to Figure 6, but for Fe II in a velocity range of $+100 \text{ km s}^{-1} < v_{\text{LSR}} < \text{LMC's disk boundary}$.

Table 5
Kendall's Tau Tests between the Angular Offsets from 30 Doradus and the Column Densities

Parameters	Fe II	Si II	O I
τ	-0.64	-0.57	-0.43
p	0.03	0.06	0.18

Note. Kendall rank correlation coefficient τ and the significance level p to measure the association between the angular offsets from 30 Doradus and the column densities.

absorbers within the velocity range of $+150 \lesssim v_{\text{LSR}} < +210 \text{ km s}^{-1}$. These values significantly exceeded the average values observed for their low-ion counterparts. The increased b -values for the high ions is mostly because they typically probe a distinct phase of the warm ionized gas compared to the low ions. Despite the generally elevated average b -values observed for high ions, a subset of components exhibits b -values $< 10 \text{ km s}^{-1}$. Such weaker narrow Si IV and C IV components could potentially indicate absorbers that are photoionized. However, there is also a possibility that they may trace nonequilibrium collision ionization (see N. Lehner et al. 2011). Additionally, the $b \gtrsim 50 \text{ km s}^{-1}$ for some of the C IV components may be an indication of more nonthermal broadening, i.e., collisions, and possibly tracing a warmer gas than Si IV. However, since the ionization potential of C IV is higher than that of Si IV, it is not surprising that they do not trace a multiphase gas in the same way. For three sightlines, namely Sk $-69^{\circ}246$, Sk $-68^{\circ}135$, and BI 173, we also possess measurements for the b -values of the intermediate-ion Al III. The average b -values and the standard deviation from the mean for the Al III ions are found to be $\langle b \rangle_{\text{Al III}} = 13.9 \pm 8.0 \text{ km s}^{-1}$. The average b -values for the Al III ions are found to lie between the values for the low ions (Fe II) and high ions (Si IV and C IV), as one would expect from the intermediate ionization potential of Al III at $\text{IP}_{\text{Al}^{+2}} = 18.8 \text{ eV}$.

6.2. Alignment of the Absorption Profiles

We compare the magnitudes of the b -values and the velocity centroids of the components between Si II and O I within the velocity range of $+100 \lesssim v_{\text{LSR}} \lesssim +220 \text{ km s}^{-1}$, which corresponds to the LMC wind region in Figure 11 (left). For the purpose of comparing the low ions with the high ions, we also

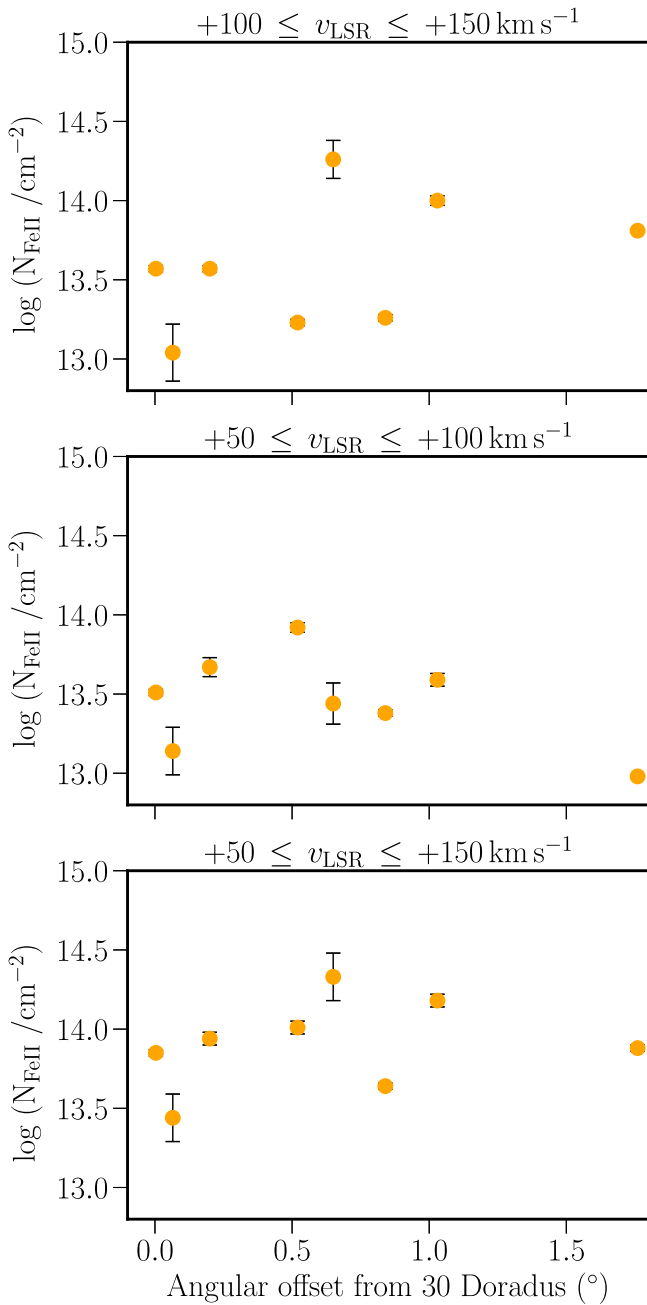


Figure 8. Variations in integrated column densities of Fe II as a function of angular separation from 30 Doradus in various velocity ranges as shown on the top of each panel.

display the b -value distributions for Si IV and Si II within the wind velocities in Figure 11 (right). In cases of complex profiles for the high ions, the application of Voigt fitting can occasionally yield excessively large b -values in order to minimize the χ^2 . The components with b -values exceeding $\sim 50 \text{ km s}^{-1}$ may be less reliable due to potential blending with other components or too low S/N and a smaller optical depth (see N. Lehner et al. 2011 for details). Therefore, we need to be careful when interpreting these broad components as they could represent either a single broad component or a composite of numerous narrower components.

Comparing the velocity centroid offsets between O I and Si II can be informative, as O I serves as a proxy for neutral hydrogen, while Si II acts as a proxy for both neutral and

ionized hydrogen. However, no significant offsets were observed between O I and Si II within the velocity range where we anticipated the presence of LMC winds. The similar b -values and the absence of significant offsets is likely due to our detection of predominantly single-phase gas in the winds probed by the low ions, which is photoionized. When comparing the positions of the components for Si II and Si IV, there are instances where they may share similar velocity centroids. However, due to the significantly higher number of components in the low ions compared to the high ions in the velocity range of the wind probed by low ions, they predominantly probe different phases of the gas. When comparing the Doppler b -values associated with matching components in Si IV and C IV, we observe that in four cases the data fall near to the nonthermal line, and in three cases they are closer to the pure thermal broadening line (see Figure 12). This implies that both thermal and nonthermal motions are important in producing the high ions.

Interestingly, we observe a consistent difference in the absorption profiles redward to the disk between low ions and high ions. In most cases, the absorption in low ions is more redshifted compared to C IV and Si IV, and also in comparison to Al III for the two systems where Al III data are available (see Figure 5 and Figure 21 in Appendix A). This effect is particularly pronounced in the closest sightlines to 30 Doradus, where we observe the most concentrated and highest-speed wind probed by low ions (see Section 5). For instance, in the BAT99 105 and Sk $-69^\circ 246$ sightlines, most of the low-ion absorption is detected beyond $v_{\text{LSR}} \gtrsim +300 \text{ km s}^{-1}$. However, for the high ions, the absorption is limited at $v_{\text{LSR}} < +300 \text{ km s}^{-1}$.

7. Gas Ionization

To evaluate the ionization state of the gas, we analyze the observed ion ratios for various low ions and the line ratios for the high ions. Additionally, we also incorporate multidimensional photoionization models using the radiative transfer code CLOUDY (version 22.01; M. Chatzikos et al. 2023) to characterize the physical and ionization properties of the gas.

7.1. Low Ions

As we will discuss in Section 7.3, we lack direct measurements of H I values for most of the wind components; therefore, it is not feasible to conduct photoionization modeling for all these components. However, we can assess the spatial and kinematic variation in ionization and dust by comparing multiple low-ionization species ratios and checking for any associated trends (see N. Lehner et al. 2009). For this exploration, we used the [Si II/O I], [Fe II/O I], and [Si II/S II] ion ratios, which are logarithmic with respect to the solar abundances. We adopt the solar abundances from the M. Asplund et al. (2009) catalog. We present those results in Table 7 for different sightlines across a range of velocities. When we observe saturation or nondetection of an ion, we report only the corresponding limits. For S II, we rely on either S II $\lambda 1250$ or S II $\lambda 1253$, while excluding S II $\lambda 1259$ due to significant blending with the Si II $\lambda 1260$ line. It is important to note that the S II $\lambda 1250$ and S II $\lambda 1253$ lines are weaker transitions and are primarily detected in the slower-moving portions of the wind, which are kinematically closer to the LMC's disk ($v_{\text{LMCSR}} > -160 \text{ km s}^{-1}$). The mean and dispersion values for [Si II/O I] and [Fe II/O I] for the

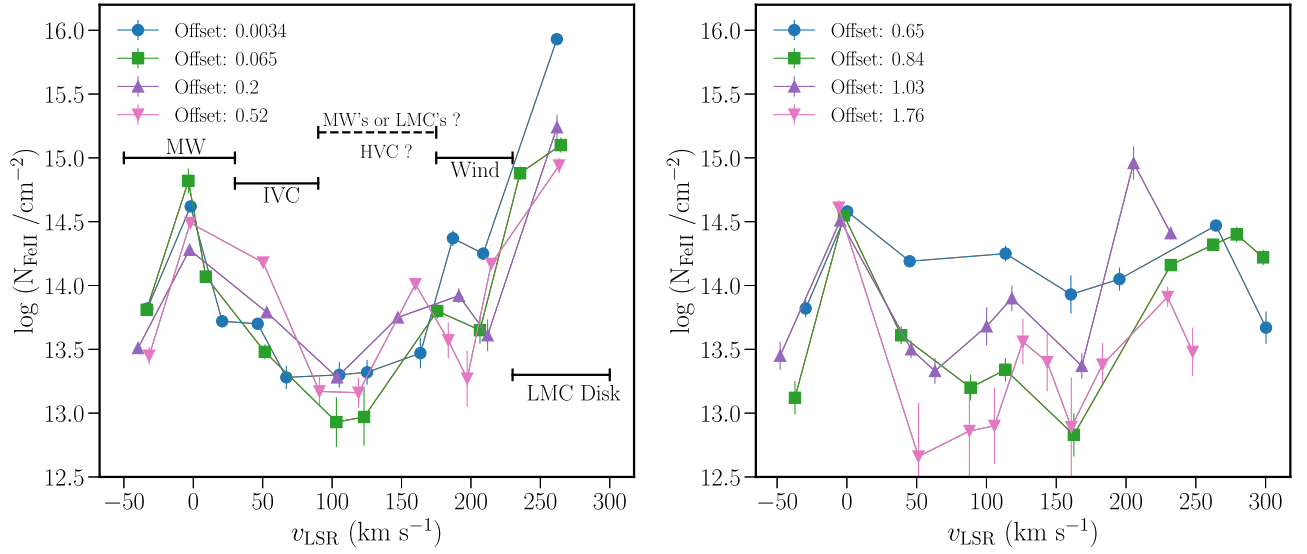


Figure 9. Variations in component column densities derived from Voigt profile fitting for Fe II with respect to v_{LSR} . The left panel includes only the first four sightlines which are within an angular separation $\lesssim 0.52^\circ$ from the center of 30 Doradus, and the right panel includes the sightlines with an offset angle $\gtrsim 0.65^\circ$. In the left panel, the different horizontal solid lines in black show the expected velocity ranges for the MW, IVCs, wind, and the LMC disk regions. The dashed line in black shows the velocity range which may be associated with the MW HVCs or the LMC wind.

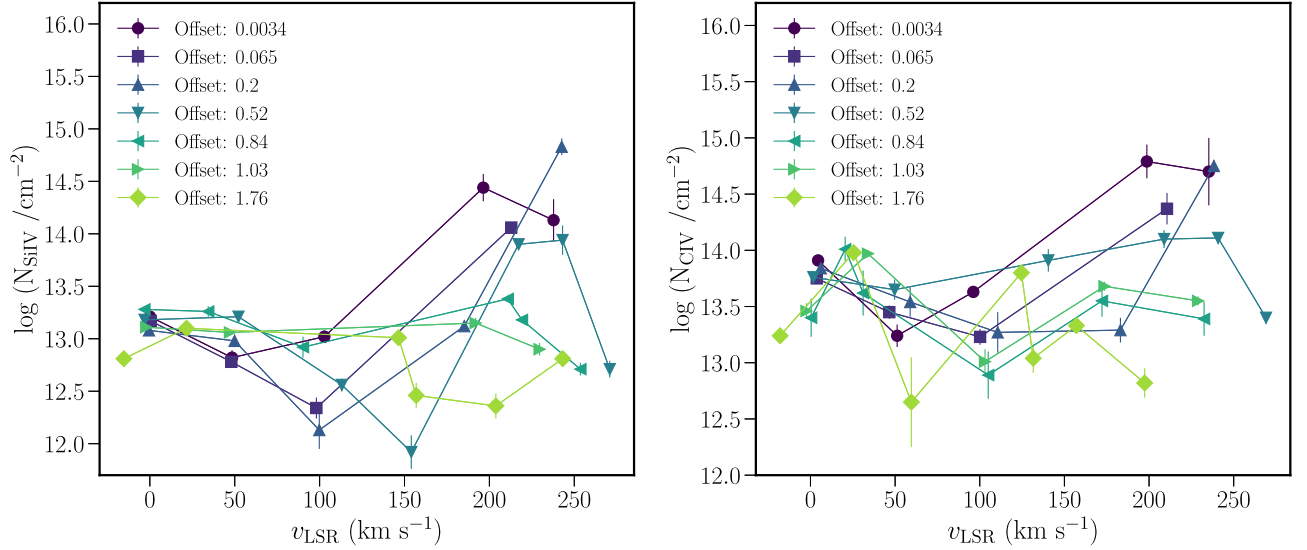


Figure 10. Variations in component column densities of Si IV (left) and C IV (right) with respect to v_{LSR} for all the sightlines for which we have Si IV and C IV measurements.

Table 6
b-value Distributions

Region	$\langle b_{\text{Fe II}} / \text{km s}^{-1} \rangle$	$\langle b_{\text{C IV}} / \text{km s}^{-1} \rangle$	$\langle b_{\text{Si IV}} / \text{km s}^{-1} \rangle$
(I)	11.1 ± 3.9
(II)	8.3 ± 3.4
(III)	11.6 ± 7.7	24.9 ± 15.2	18.4 ± 11.9
(IV)	11.8 ± 5.1

Note. The values given in the second, third, and fourth columns are (average \pm standard deviation) of the *b*-values for different regions based on the expected LMC wind region deduced from Section 5: Milky Way (Region I: $v_{\text{LSR}} < 100 \text{ km s}^{-1}$), Region II: $100 \text{ km s}^{-1} < v_{\text{LSR}} < 150 \text{ km s}^{-1}$, LMC winds (Region III: $150 \text{ km s}^{-1} < v_{\text{LSR}} < 210 \text{ km s}^{-1}$), and LMC disk (Region IV: $v_{\text{LSR}} > 210 \text{ km s}^{-1}$) for various ions.

components at $v_{\text{LSR}} \gtrsim +100 \text{ km s}^{-1}$ are 0.73 ± 0.29 and 0.43 ± 0.25 dex, respectively. These dispersions substantially exceed the measurement errors for individual components, indicating the presence of genuine variations in ionization or dust depletion conditions across different sightlines and components. However, we do not find a clear trend in the [Si II/O I] and [Fe II/O I] values concerning their proximity to the 30 Doradus region. Also, there is not a discernible pattern of these values kinematically. Below, we discuss the potential factors, such as ionization or dust depletion effects, which may be contributing to these variations in the ion ratios.

To accurately interpret ion ratios, we consider three fundamental properties of atomic species: chemical evolution, ionization, and dust depletion. Iron, for instance, is primarily produced during

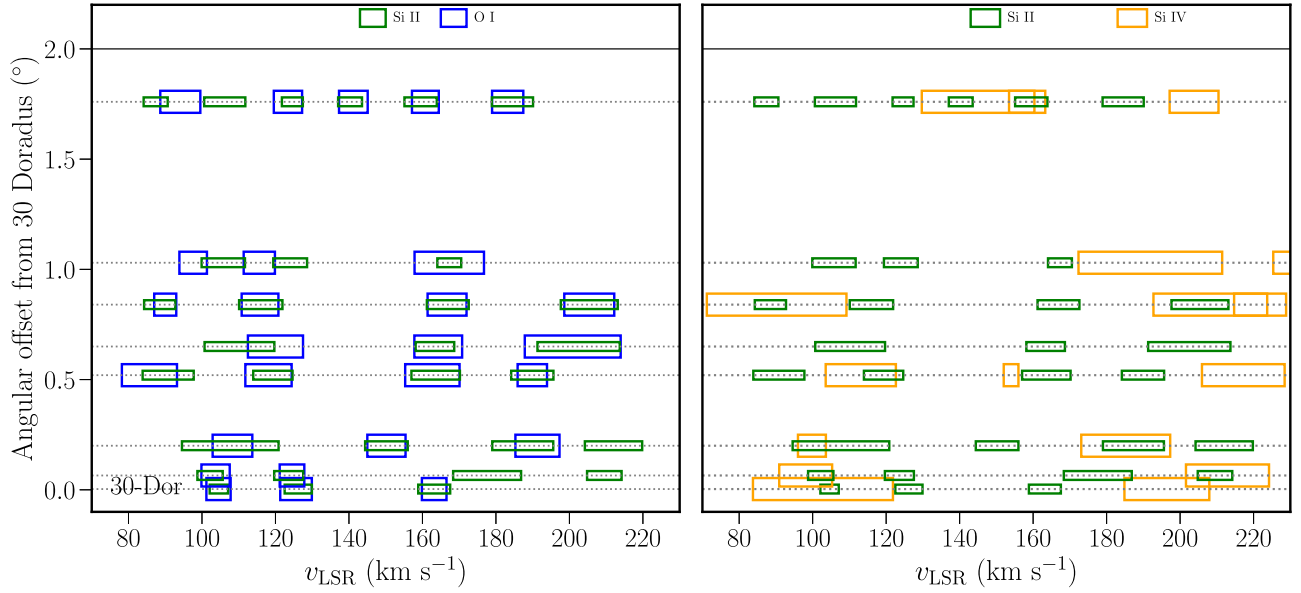


Figure 11. Comparisons of Doppler b -parameters distributions across various sightlines at varying angular separations from 30 Doradus. Left: between the low ions Si II and O I in the range of $+90 \lesssim v_{\text{LSR}} \lesssim +220 \text{ km s}^{-1}$. Right: between the high ions Si IV and the low ions Si II. In both figures, the widths of the rectangular boxes are equal to the magnitudes of the Doppler b -parameters, while the varying heights of the boxes are intentionally adjusted to enhance visibility. The centers of these boxes represent the velocity centroids of the individual components. The horizontal dotted lines indicate the angular separations of these sightlines from the center of 30 Doradus.

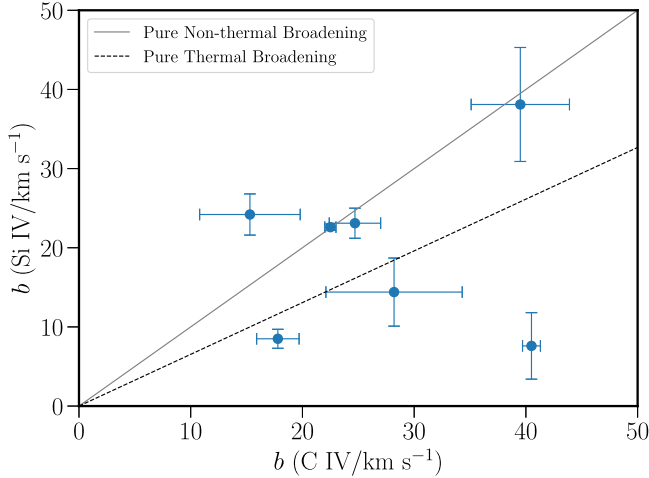


Figure 12. Comparison of the b -parameters for the velocity-matching components between Si IV and C IV that fall within $90 \text{ km s}^{-1} \lesssim v_{\text{LSR}} \lesssim 220 \text{ km s}^{-1}$. The solid line in gray is the broadening due to pure nonthermal motion, and the dashed line in black is the broadening assuming a pure thermal motion.

Type I supernova explosions (K. Nomoto et al. 1997), while Type II supernovae produce α elements along with iron (K. Nomoto et al. 2006). These distinct phenomena may cause variations in the quantities of atomic species they disperse into the ISM. For example, an α -element enhancement of ~ 0.26 dex is observed in the neutral ISM in the LMC (A. De Cia et al. 2024). Therefore, given the disparate timescales of these phenomena and the variations they produce in the abundances of atomic species, it is crucial to focus on elements with similar chemical evolution when interpreting ion ratios. Moreover, the dust depletion level depends on different density environments and may also correlate with the metallicity (see A. De Cia et al. 2024 and references therein). Furthermore, dust depletion patterns differ for refractory elements like silicon and iron compared to volatile elements like sulfur, oxygen, and phosphorus (B. D. Savage & K. R. Sembach 1996;

E. B. Jenkins 2009; E. B. Jenkins & G. Wallerstein 2017). Silicon and iron are subject to more extensive depletion than oxygen and sulfur in the MW's ISM (E. B. Jenkins 2009). Since silicon and oxygen are both α elements, the [Si II/O I] ratio should remain largely unaffected by chemical evolution. However, this ratio is influenced by dust and ionization effects. Oxygen being a volatile element, we do not anticipate significant dust depletion (E. B. Jenkins 2009), and the ionization correction for oxygen is also minimal (S. M. Viegas 1995). Therefore, to interpret [Si II/O I], we must weigh the relative impact of dust depletion versus ionization on Si II. In general, if moderate dust depletion is expected in HVC gas, we might anticipate $-0.3 \lesssim [\text{Si II/O I}] \lesssim 0.0$ dex (see also N. Lehner et al. 2009). For example, A. J. Fox et al. (2023) found the dust depletion for HVC Complex C to be $\delta(\text{Si}) \approx -0.29$ dex, suggesting moderate dust depletion. Therefore, our observed average value of $[\langle \text{Si II/O I} \rangle] = 0.73 \pm 0.29$ dex is primarily driven by the ionization of Si II, with the considerable dispersion in values stemming from spatial and kinematic ionization variations (see N. Lehner et al. 2009). We also estimate the ionization fraction by using O I as a proxy for neutral hydrogen and Si II as a substitute for both neutral and ionized hydrogen (H I+H II; see N. Lehner et al. 2009, 2001; K. A. Barger et al. 2016). The hydrogen ionization fraction can be approximated using the following equation:

$$\chi_{\text{H II}} = 1 - \chi_{\text{H I}} \quad (4)$$

$$> 1 - \frac{N_{\text{OI}}}{N_{\text{Si II}}} \cdot \frac{(\text{Si/H})_{\odot}}{(\text{O/H})_{\odot}}, \quad (5)$$

where the hydrogen ionization fraction is $\chi_{\text{H II}} = N_{\text{H II}}/(N_{\text{H I}} + N_{\text{H II}})$, the fraction of neutral hydrogen is $\chi_{\text{H I}}$, and $(\text{Si/H})_{\odot}$ and $(\text{O/H})_{\odot}$ represent the solar abundance of silicon and oxygen, respectively. Using this method, we estimated the hydrogen ionization fraction of the absorbers along our eight sightlines, which we display in Figure 13. We include only components which have both the O I and Si II

Table 7
Observed Ion Ratios

Sightline	Angular Offset (deg)	v_{LSR} (km s ⁻¹)	[Fe II/O I]	[Si II/O I]	[Si II/S II]	Comments
BAT99 105	0.003	+104.5	0.37 ± 0.10	0.38 ± 0.06	> -0.79	HVC/wind
		+125.6	0.45 ± 0.10	0.46 ± 0.07	> -0.68	HVC/wind
		+163.2	0.63 ± 0.17	0.52 ± 0.18	-0.96 ± 0.27	LMC wind
Sk - 69°246	0.06	+103.7	0.28 ± 0.05	0.61 ± 0.06	> -0.78	HVC/wind
		+124.5	0.45 ± 0.07	0.81 ± 0.08	> -0.69	HVC/wind
		+177.6	> 0.14	LMC wind
		+209.5	-0.13 ± 0.20	LMC wind
Sk - 68°135	0.20	+108.3	0.39 ± 0.04	1.14 ± 0.04	> -0.01	HVC/wind
		+150.2	< 0.21	< 1.12	> 0.68	LMC wind
		+191.3	< 0.19	< 1.18	0.03 ± 0.14	LMC wind
		+212.0	0.49 ± 0.36	LMC wind
BI 214	0.52	+85.7	-0.09 ± 0.12	0.43 ± 0.08	> 0.17	HVC/wind
		+118.1	0.07 ± 0.13	0.55 ± 0.06	> -0.25	HVC/wind
		+162.7	< 0.21	...	> -0.39	LMC wind
		+189.9	> -0.25	LMC wind
Sk - 69°175	0.65	+120.0	0.24 ± 0.07	0.60 ± 0.17	-0.48 ± 0.18	LMC wind ^a
		+164.3	0.52 ± 0.23	0.17 ± 0.27	...	LMC wind
		+200.9	-0.02 ± 0.11	0.30 ± 0.07	-0.74 ± 0.08	LMC wind
Sk - 68°112	0.84	+90.0	0.35 ± 0.12	0.77 ± 0.07	> -0.25	HVC/wind
		+116.6	< 0.13	...	> -0.01	HVC/wind
		+166.6	0.17 ± 0.17	0.90 ± 0.04	-0.81 ± 0.12	LMC wind
		+205.4	< -0.21	0.76 ± 0.06	-0.60 ± 0.23	LMC wind
BI 173	1.03	+115.6	0.08 ± 0.09	> -0.04	> 0.11	MW HVC ^a
		+167.3	-0.76 ± 0.18	LMC wind
Sk - 69°104	1.76	+94.1	0.07 ± 0.30	0.70 ± 0.19	> -0.38	HVC/wind
		+123.4	0.48 ± 0.18	0.62 ± 0.11	> 0.12	HVC/wind
		+141.2	0.35 ± 0.23	0.79 ± 0.08	> -0.03	HVC/wind
		+160.8	0.15 ± 0.39	0.83 ± 0.09	> -0.41	LMC wind
		+183.2	0.74 ± 0.08	0.91 ± 0.06	> -0.58	LMC wind

Notes. This table shows the ion ratios for the matching components in a velocity range of $+90 \text{ km s}^{-1} \lesssim v_{\text{LSR}} < \text{LMC's disk boundary}$. For most of the components, the v_{LSR} values are provided based on the velocity centroids for O I. However, when a reliable O I measurement is not available, we provide this value based on Si II. Sightlines are ordered in the increasing angular offsets from the center of 30 Doradus. The comments in the final column indicate the association of these absorption components with either the MW HVCs, the LMC wind, or a combination of HVCs and wind when a distinct connection with the MW HVCs and/or LMC wind is not evident. For all of the sightlines, the absorption at $v_{\text{LSR}} > 150 \text{ km s}^{-1}$ is most likely associated with the LMC wind based on the discussion in Section 5. The absorption at $+100 \text{ km s}^{-1} \lesssim v_{\text{LSR}} \lesssim +150 \text{ km s}^{-1}$ does not have a clear association with the MW HVCs or the LMC wind, except for two components in two sightlines where the photoionization modeling is available.

^a Based on the photoionization modeling from Section 7.3.

detections. Generally, we observe that the wind components are ionized to varying degrees, ranging from at least 40% to as high as 90% based on the observation. It is important to note that if silicon is depleted relative to oxygen, the estimated [Si II/O I] would provide a lower limit, and the gas could be even more ionized. The data uncover both spatial and kinematic anisotropy in the ionization fractions. However, no clear trend in the ionization fraction concerning the distance from 30 Doradus is evident.

To examine how the hydrogen ionization fraction varies across different velocity regimes, we compute their weighted averages in three distinct velocity bins. For the absorbers across all eight sightlines, we find that $\langle \chi_{\text{H II}} \rangle = 0.87 \pm 0.03$ at $v_{\text{MW,disk}} < v_{\text{LSR}} \leq +100 \text{ km s}^{-1}$, $\langle \chi_{\text{H II}} \rangle = 0.72 \pm 0.11$ at $+100 \leq v_{\text{LSR}} < +150 \text{ km s}^{-1}$, and $\langle \chi_{\text{H II}} \rangle = 0.76 \pm 0.14$ at $+150 \text{ km s}^{-1} \leq v_{\text{LSR}} < v_{\text{LMC,disk}}$. Notably, the ionization fraction of the gas at $v_{\text{LSR}} < +100 \text{ km s}^{-1}$ that likely traces MW material is higher than and does not overlap with the gas moving at $+100 \leq v_{\text{LSR}} < +150 \text{ km s}^{-1}$. However, the ionization fraction of the gas moving at this intermediate-velocity bin does overlap with the highest-velocity bin material

that is moving at speeds more closer with the LMC, albeit the latter has a much larger spread. The overlap between these two may indicate a causal connection between the gas in these two velocity bins that would be speculated if they shared the same physical origin. One might expect the LMC wind to be highly ionized due to the stellar feedback that heats the gas through a combination of photoionization and shock heating. However, other factors—such as mixing with the surrounding media—could promote cooling. Combined, this has led to a large spread in ionization conditions in this region.

Another crucial ion ratio to consider is [Si II/S II]. Since both silicon and sulfur are α elements, this ratio depends on the relative effects of dust and ionization. We compare the distribution of this ratio across various offsets from 30 Doradus and a wide range of velocities (see Figure 14). In the cases of saturation of the Si II lines and nondetection of S II lines, we present the lower limit of the ratio, shown by the upward-directed triangle. While there is not a distinct dependence of [Si II/S II] on velocity, a noticeable trend emerges regarding projected distance from 30 Doradus, especially for slow-moving components. Sightlines in close proximity to 30 Doradus tend to exhibit solar or occasionally supersolar values,

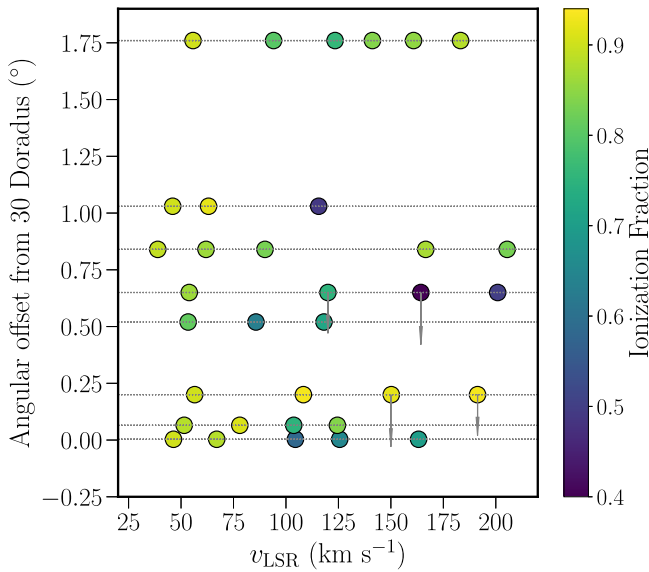


Figure 13. Ionization fraction as a function of angular separation from the 30 Doradus region and v_{LSR} as determined by employing O I as a proxy for neutral hydrogen and Si II as a substitute for neutral and ionized hydrogen. Only components where both O I and Si II were detected are included in the analysis. In a few cases, the upper limits in the values are depicted by the downward-directed arrows. The horizontal dotted lines are drawn at the corresponding angular separations of these sightlines from the center of 30 Doradus.

while those farther away predominantly have subsolar values. If we consider sulfur as an undepleted element due to its lower condensation temperature, the ratio might suggest a depletion pattern that resulted from more dust destruction in the central region of 30 Doradus by the higher number of SNRs (see M. Lakićević et al. 2015). However, we cannot draw a conclusion from this ratio alone without considering the ionization state of the gas, as the ionization potential for S II is higher than that of Si II. Additionally, recent studies indicate that there is evidence of sulfur depletion in the ISM (J. Roman-Duval et al. 2022).

7.2. High Ions

While the neutral and low-ionization atomic species trace the neutral and photoionized outflows from the LMC, the high ions, C IV and Si IV, may probe both the photoionized and collisionally ionized gas. The theoretical models describing the ionization mechanisms responsible for generating the high ions present varying predictions for their ratios (L. Spitzer 1996). The column density ratios of C IV and Si IV have been widely used to understand the physical and ionization conditions in both the MW and the LMC (N. Lehner et al. 2011; K. A. Barger et al. 2016; J. K. Werk et al. 2019; D. Krishnarao et al. 2022). To accurately estimate the ratios, it is imperative that the Si IV and C IV ions exhibit similar velocity structures and velocity centroids. Across the first three sightlines, two components each have matching counterparts between Si IV and C IV within the velocity range of $+90 \lesssim v_{\text{LSR}} \lesssim +220 \text{ km s}^{-1}$. However, the outer sightlines generally lack matching pairs for both ions. We compare the column density ratios for these matching components as a function of C IV column density and $b_{\text{C IV}}$ (see Figure 15). We observe that the higher values of $N_{\text{C IV}}/N_{\text{Si IV}}$ are typically associated with higher values of $b_{\text{C IV}}$. We estimate that C IV and Si IV ions sharing identical velocities exhibit a mean and dispersion of $\langle N_{\text{C IV}}/N_{\text{Si IV}} \rangle = 3.7 \pm 2.3$, with values

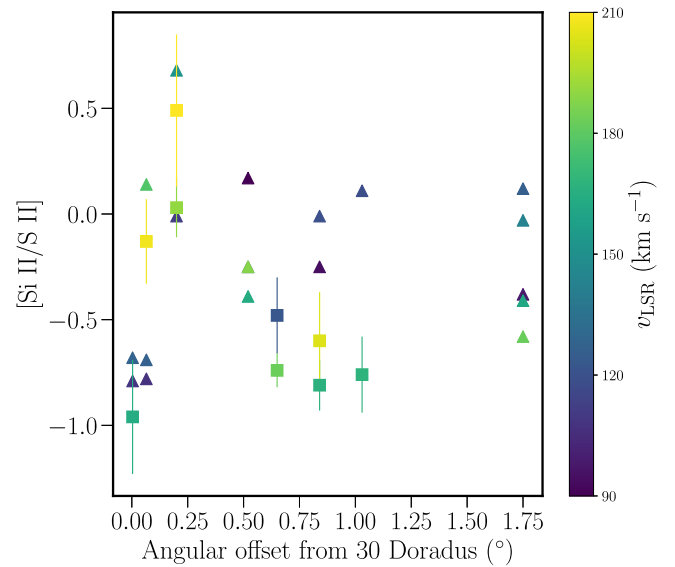


Figure 14. Variation of $[\text{Si II/S II}]$ with offset angle from 30 Doradus and v_{LSR} . The upward-directed triangles without the error bars are only the lower limits.

spanning from 1.5 to 7.8. Our $N_{\text{C IV}}/N_{\text{Si IV}}$ ratios and values of $b_{\text{C IV}}$ do not suggest that photoionization alone is influencing this gas, as incident ionizing radiation is anticipated to produce more $N_{\text{Si IV}}$ than $N_{\text{C IV}}$ due to the much lower ionization potential of the silicon ions at $\text{IP}_{\text{Si}^{3+}} = 33.5 \text{ eV}$ compared to $\text{IP}_{\text{C}^{3+}} = 47.9 \text{ eV}$. Instead, this average ratio indicates a preference for collisional ionization, with turbulent mixing layers (TMLs; K. Kwak et al. 2015; R. L. Shelton & K. Kwak 2018) which exist in the wind appearing to be the best candidates for the production of these high ions (see N. Lehner et al. 2011).

We also analyzed the line ratios for all sightlines that have well-behaved continuum (seven out of eight) over velocities that span from the MW to the LMC ($v_{\text{LSR}} = -20$ to $+300 \text{ km s}^{-1}$) by estimating the AOD column density for Si IV and C IV in discrete 40 km s^{-1} bins (see Figure 16). While these ratios vary among different sightlines, we generally observe that they are larger for the MW region than for the LMC. To compare them further, we plotted the mean values for these ratios for each sightline with a dotted line. For many of the sightlines, the ratios for the bins located at $v_{\text{LSR}} > +150 \text{ km s}^{-1}$ are smaller than the mean value, possibly suggesting their association with the LMC. In N. Lehner & J. C. Howk (2007), they observed that the line ratios of O VI and C IV vary from sightline to sightline. However, they also found that the MW and IVC components had similar ratios and that the HVC and LMC components ratios were similar, suggesting two different associations. If we compare our global mean $N_{\text{C IV}}/N_{\text{Si IV}}$ ratios across all sightlines for each velocity bin, the ratio reaches its maximum at the bin center of $v_{\text{LSR}} = +80 \text{ km s}^{-1}$ and then decreases toward the LMC, suggesting a transition region somewhere between $+80 \lesssim v_{\text{LSR}} \lesssim +120 \text{ km s}^{-1}$. While the physical meaning of this trend is unclear, it might indicate a transition similar to what we observed in Section 5.2 for the column density versus velocity of Fe II.

Our photoionization models (which we discuss in more detail in Section 7.3) for the $v_{\text{LSR}} = +115 \text{ km s}^{-1}$ component along sightline BI 173 and the $v_{\text{LSR}} = +120 \text{ km s}^{-1}$ component along sightline Sk $-69^\circ 175$ also predict the column densities of Si IV and C IV in single-phase photoionized gas in which the

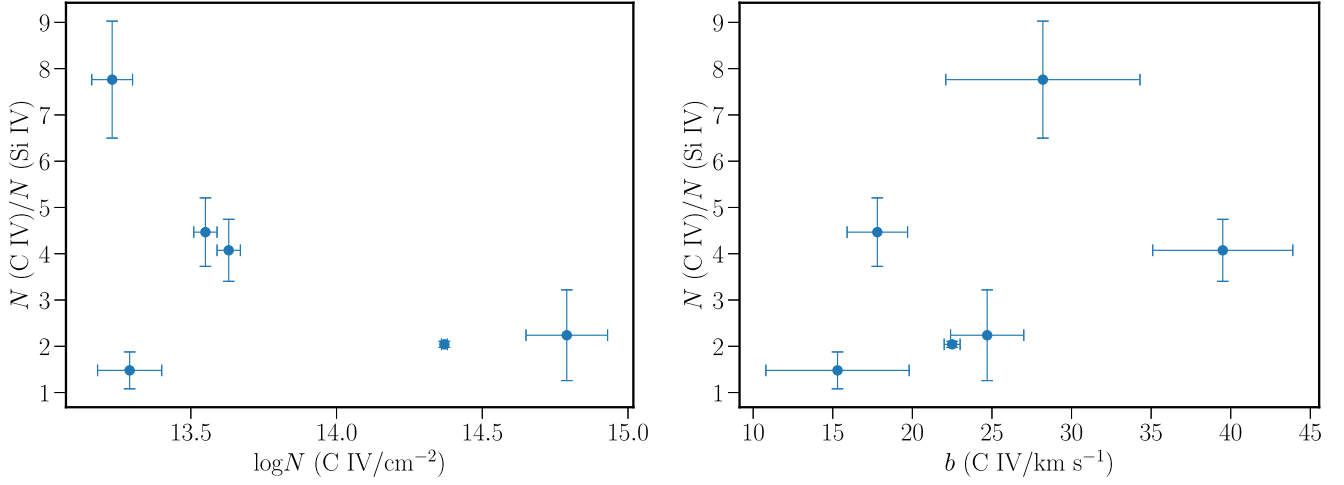


Figure 15. Ratio of C IV and Si IV column densities for the velocity-matching components that fall within $90 \text{ km s}^{-1} \lesssim v_{\text{LSR}} \lesssim 220 \text{ km s}^{-1}$ (a) as a function of $\log N$ C IV (left) and (b) as a function of b -values for C IV (right).

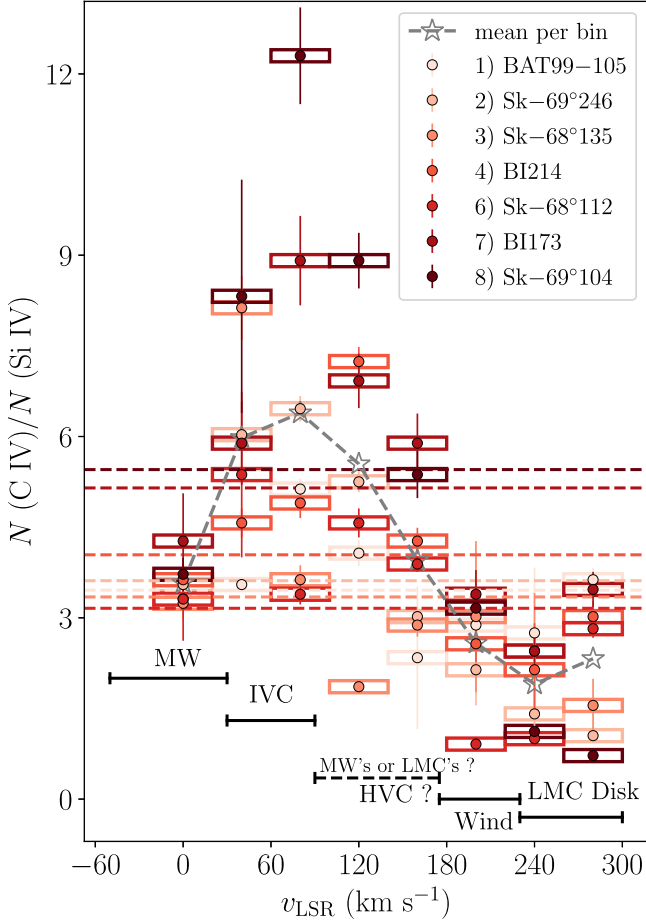


Figure 16. Ratio of C IV and Si IV AOD column densities for eight different bins between $v_{\text{LSR}} = -20$ to $+300 \text{ km s}^{-1}$, with each bin size equal to 40 km s^{-1} , indicated by the span of the horizontal bars. The mean values for these ratios for each sightline over the entire sampled velocity range are represented with a horizontal dotted line. Darker red colors represent sightlines farther from the center of 30 Doradus, while lighter shades correspond to closer sightlines. Additionally, we plot the mean values across all sightlines for each velocity bin, represented by gray stars, and connect these points with a dashed gray line. Similar to Figure 9, the different horizontal solid lines in black mark the expected velocity ranges for the MW, IVCs, wind, and the LMC disk regions, and the dashed black line marks the velocity range which may be associated with either the MW's HVCs or the LMC wind.

low and high ions are well mixed. For the Sk $-69^\circ 175$ sightline, the modeled photoionized column densities are $\log(N_{\text{SiIV}}/\text{cm}^{-2}) = 14.24$ and $\log(N_{\text{CIV}}/\text{cm}^{-2}) = 14.77$. For this component, the model predicts that the dominant phases for silicon and carbon are in the form of Si III and C III. However, we lack the observed column densities of Si IV and C IV for this sightline to compare with the predictions. For the BI 173 sightline, the predicted photoionized Si IV and C IV column densities are extremely small, at $\log(N_{\text{SiIV}}/\text{cm}^{-2}) = 8.86$ and $\log(N_{\text{CIV}}/\text{cm}^{-2}) = 7.37$. The much larger observed value of $\log(N_{\text{SiIV}}/\text{cm}^{-2}) = 13.02$ for a component at a similar velocity suggests that photoionization alone cannot account for such a high column density for Si IV, and therefore requires a higher contribution from the nonthermal motion of the gas. From the average Doppler parameter values for the Si IV and C IV, we estimate that the gas probed by these ions can reflect temperatures of $T < 8.5 \times 10^5 \text{ K}$ and $< 6.9 \times 10^5 \text{ K}$, respectively, suggesting TMLs being the most likely candidates of these high ions. However, these ions may also be indicative of probing the corona of the LMC or an interface region where the wind feeds into the LMC's halo.

7.3. Photoionization Modeling

While the observed ion ratios in Section 7.1 provide some insight into the ionization conditions, we further assess the physical and ionization properties through photoionization modeling. The neutral and low-ionization species, i.e., O I, Si II, S II, Al II, and Fe II, with narrow component structure should trace the cool photoionized phase of the LMC's outflow. We observe multiple components of neutral, low, and intermediate ions in each of our sightlines between the MW and the LMC; however, the location of these components is not known for certain. Components observed at $v_{\text{LSR}} \geq +100 \text{ km s}^{-1}$ can be associated with MW halo HVCs as well as with the LMC wind. Given the discussion in Sections 3.3, 3.4, and 5.2 above, and that we are looking in the direction of an active star-forming region, we explore if blueshifted absorbers that are kinematically offset from the LMC's H I disk by more than 100 km s^{-1} could be part of a high-velocity outflow from the LMC. For example, this would include the $v_{\text{LSR}} \approx +120 \text{ km s}^{-1}$ ($v_{\text{LMCSR}} \approx -152 \text{ km s}^{-1}$) components along the Sk $-69^\circ 175$ sightline.

To assess the role of photoionization in these components, as well as to characterize their physical conditions and element abundances, we include multidimensional photoionization models using CLOUDY (M. Chatzikos et al. 2023) in our analysis. These models aim to (i) provide measurements of unseen ion stages in order to determine an elemental abundance, (ii) quantify the amount of dust depletion, and (iii) provide a constraint on the size and location of the cloud. All models assume that the outflow component is a plane-parallel slab of uniform density exposed to radiation fields from the MW disk, Magellanic Clouds, and extragalactic background. We did not use the direct radiation field from the 30 Doradus star-forming region, as exposing these fast-moving clouds with a velocity of $v_{\text{LSR}} \approx +120 \text{ km s}^{-1}$ to such field does not reproduce the observed H I and O I column densities as all of the oxygen and hydrogen will be ionized under such exposure. The MW disk-halo model that we used is a nonisotropic composite hard and soft radiation field composed from the escaping UV flux of O–B stars (J. Bland-Hawthorn & P. R. Maloney 1999; A. J. Fox et al. 2005, 2014; J. Bland-Hawthorn et al. 2019). The Magellanic radiation fields from K. A. Barger et al. (2013) are rotated versions of the MW’s model that have been rescaled so they match the observation of H α emission toward the Magellanic Bridge. We adopt the extragalactic UV background from V. Khaire & R. Srianand (2019). With this coadded and 3D reconstructed radiation field, we were able to interpolate its strength at any distance between the MW and LMC.¹⁶

As we do not know the precise position of the gas along the line of sight, we run our models over a large grid of flux values that correspond to different physical positions between the MW and LMC. Following the presentation of the disk-halo model in J. Bland-Hawthorn et al. (2019), an absorber along the line of sight to the LMC could be exposed to an escaping hydrogen-ionizing flux in the range of $4.65 \lesssim \log(\Phi_{\text{H}}/\text{photons cm}^{-2} \text{ s}^{-1}) \lesssim 7.05$. We therefore ran all of our CLOUDY photoionization models over this flux range in step sizes of 0.15 dex to match the contours of the model (see J. Bland-Hawthorn et al. 2019). Thus, this modeling approach will ascertain what range of flux values is permitted by the observations to help narrow down the physical location of the cloud components along the line of sight. We ran each of these models over a range of hydrogen number densities from $-3 \leq \log(n_{\text{H}}/\text{cm}^{-3}) \leq 0$ in steps of 0.1 dex.

We are only able to perform photoionization modeling for high-velocity components toward two LMC stars, Sk – 69°175 and BI 173, as they have suitable H I emission data, which serves as the model stopping criteria since H I should be cospatial with our most robust metallicity tracers, O I and S II. For our purposes, suitable H I data are detections of at least 3σ that are similar velocities to the observed neutral and low-ion species. Details and results for each sightline are described in the following subsections.

7.3.1. The +115 km s^{−1} Component toward BI 173

We observe an absorption component of O I at $v_{\text{LSR}} = +115.6 \text{ km s}^{-1}$ in the STIS UV spectrum toward BI 173 that kinematically overlaps with the H I 21 cm emission centered at $v_{\text{LSR}} = +117.9 \text{ km s}^{-1}$ (see Figure 21). Corresponding

components for Si II, Fe II, and Al II are also observed within the velocity range of $+118 \leq v_{\text{LSR}} \leq +124 \text{ km s}^{-1}$. However, this component does not have an adjacent ion ratio to constrain the ionization parameter, therefore we designed a CLOUDY optimization model to find model parameters that are consistent with the observed column densities in this component (see Table 3).

We use CLOUDY’s built-in `optimize` command with two free parameters: the hydrogen-ionizing photon flux Φ_{H} and the total hydrogen number density n_{H} . As described above, these initial broad range requirements ensure that CLOUDY does not settle at a local minima during the optimization process. The neutral hydrogen column density measured in this component ($\log(N_{\text{HI}}/\text{cm}^{-2}) = 19.01 \pm 0.10$ from the GASS survey) serves as our stopping criterion. Because H I and O I are known in this component, we use the $[\text{O I}/\text{H I}] = -0.69 \pm 0.13$ dex abundance as an additional input parameter. We want to emphasize that this value of $[\text{O I}/\text{H I}]$ is in excellent agreement with the value estimated by N. Lehner et al. (2009). To fine-tune the optimization model even further, we permit this metallicity to vary within a margin of error of ± 0.15 dex in 0.05 dex increments. After the optimization model returns the optimal $\log \Phi_{\text{H}}$, $\log(n_{\text{H}})$, and metallicity, we run a final CLOUDY model at those parameters to determine the best-matched model predicted ion column densities, ionization corrections, and potential dust depletion.

The results of the optimization model describe a cloud that is predominately neutral, with $\log(N_{\text{HI}}/\text{cm}^{-2}) = 18.31$ and a hydrogen ionization fraction of $\chi_{\text{H II}} = 0.17$. We find an optimal hydrogen number density and hydrogen-ionizing photon flux of $\log(n_{\text{H}}/\text{cm}^{-3}) = -0.29$ and $\log(\Phi_{\text{H}}/\text{photons cm}^{-2} \text{ s}^{-1}) = 5.16$. The characteristic thickness of the absorbing neutral gas layer is 6.5 pc, calculated from the hydrogen number density and the neutral gas column density, i.e., $r = N_{\text{HI}}/n_{\text{H}}$. Thus, the model predicts a small, mostly neutral cloudlet with $\log(T/\text{K}) \approx 3.8$. Since this absorber lies somewhere along the line of sight between the star BI 173 in the LMC and the Sun, exposure to this ionizing photon flux places the receding cloud at a radial distance of either 7.5 kpc from the center of the LMC or 4.3 kpc from our position in the disk of the MW.

Because the ionic column density we observe may not be the dominant ion stage present in the gas, we utilize the model results to calculate ionization corrections for the observed ion stages. The ionization correction can be expressed as a difference between the true and observed ion abundance, i.e.,

$$\text{IC}(X^i) = [X/\text{H}] - [X^i/\text{H I}]. \quad (6)$$

We find a low-ionization correction of $\text{IC}(\text{O}) = -0.01$, which results in a low gas-phase oxygen abundance of $[\text{O}/\text{H}] = -0.70 \pm 0.13$ dex. We calculate ionization-corrected gas-phase abundances of $[\text{Al}/\text{H}] \geq -0.74$, $[\text{Si}/\text{H}] \geq -0.81$, and $[\text{Fe}/\text{H}] = -0.68 \pm 0.12$ dex (see Table 8 and the top and middle panels of Figure 17). The error bars on the ionization corrections in the top panel represent the highest and lowest possible correction to the ion abundance if the model column density (i.e., O I, Al II, Si II, or Fe II) were 10% higher or lower. We include this range to demonstrate the low sensitivity this change has on the ionization correction. This range of sensitivity is also propagated through to the calculated element abundance and the associated error.

We check for dust depletion effects in this component following the convention that the depletion, $\delta_{\text{O}}(X)$, of a

¹⁶ The Milky Way Radiation Field and Ionization Photon Flux Tool, which includes contributions from the Magellanic Clouds: <https://github.com/Deech08/galrad>.

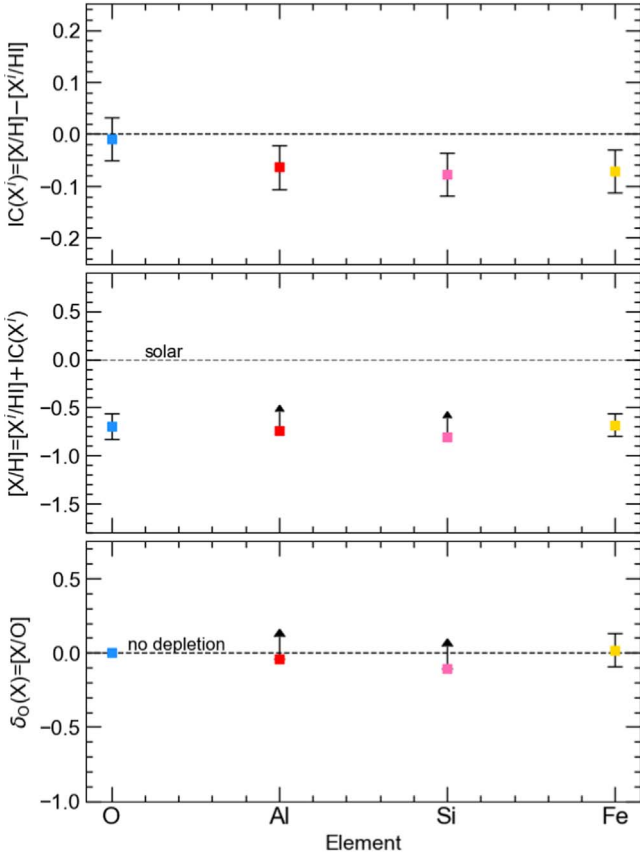


Figure 17. Photoionization modeling results for the $v_{\text{LSR}} \approx +115 \text{ km s}^{-1}$ component toward BI 173 with optimal hydrogen number density $\log(n_{\text{H}}/\text{cm}^{-3}) = -0.29$ and hydrogen-ionizing photon flux of $\log(\Phi_{\text{H}}/\text{photons cm}^{-2} \text{ s}^{-1}) = 5.16$. Top panel: ionization corrections for the low ions O I, Al II, Si II, and Fe II. The dashed gray horizontal line at zero indicates no ionization correction. Middle panel: comparison of the elemental abundances after correcting the ionization. The dashed gray horizontal line at zero marks the solar abundance. Bottom: comparison of the levels of depletion among different elements $\delta_{\text{O}}(X) = [X/O]$. The dashed gray horizontal line at zero indicates no depletion relative to oxygen.

Table 8

Summary of Photoionization Modeling Results for $v_{\text{LSR}} \approx +115 \text{ km s}^{-1}$ Component toward BI 173

Element (X)	IC (X^i)	[X/H]	$\delta_{\text{O}}(X)$
O	-0.01 ± 0.04	-0.70 ± 0.13	...
Al	-0.06 ± 0.04	≥ -0.74	≥ -0.04
Si	-0.08 ± 0.04	≥ -0.81	≥ -0.11
Fe	-0.07 ± 0.04	-0.68 ± 0.12	-0.02 ± 0.11

refractory element X is measured as a difference between ionization-corrected abundances of X and oxygen:

$$\delta_{\text{O}}(X) \equiv [X/H] - [O/H]. \quad (7)$$

A negative value for $\delta_{\text{O}}(X)$ indicates depletion of X with respect to the volatile element oxygen, under the assumption that the total (gas + dust) abundances are solar. The error for the depletion depends only on the observed ion column density errors and the IC sensitivity values for the refractory and volatile elements. Overall, we find a lower limit for the depletion level for both silicon and aluminum of $\delta_{\text{O}}(\text{Si}) \geq -0.11$ and $\delta_{\text{O}}(\text{Al}) \geq -0.04$ dex, respectively. We find

$\delta_{\text{O}}(\text{Fe}) = -0.02 \pm 0.11$ dex (see Table 8 and the bottom panel of Figure 17). The dust depletion measurements suggest there is no dust in this cloud. Overall, these physical characteristics (i.e., mostly neutral, cool, low-metallicity, dust-free) suggest the cloud seen near $+115 \text{ km s}^{-1}$ is a MW halo HVC.

7.3.2. The $+120 \text{ km s}^{-1}$ Component toward Sk $-69^{\circ}175$

Along the Sk $-69^{\circ}175$ sightline, we observe an absorption component of O I that is centered at $v_{\text{LSR}} = +120.0 \text{ km s}^{-1}$ in the FUSE FUV spectrum that overlaps with the H I 21 cm emission line at $v_{\text{LSR}} = +116.4 \text{ km s}^{-1}$ (see Figure 21). N. Lehner et al. (2009) measured $\log(N_{\text{HI}}/\text{cm}^{-2}) = 19.18 \pm 0.10$ for this component using Parkes radio 21 cm data from the LMC H I survey (L. Staveley-Smith et al. 2003). We also observe multiple singly ionized species Al II, Si II, S II, Fe II, and Ni II that overlap and with centroids within the velocity range of $+108 \leq v_{\text{LSR}} \leq +116 \text{ km s}^{-1}$. We measure a lower limit of $\log(N_{\text{SiII}}/N_{\text{SiI}}) \geq -1.16$ dex (Si III is saturated) for this absorber, which we can use to bound the ionization parameter.

We designed a CLOUDY optimization model to find the optimal parameters that explain the observed column densities for this absorber (see Table 3). We once again use CLOUDY's built-in optimize command with free parameters Φ_{H} and n_{H} , where we used the neutral hydrogen column density measured in this component of $\log(N_{\text{HI}}/\text{cm}^{-2}) = 19.18$ dex as a model stopping criterion. The model optimizes over the range of flux values from $4.65 \leq \log(\Phi_{\text{H}}/\text{cm}^{-2} \text{ s}^{-1}) \leq 7.05$ in steps of 0.15 dex and number density $-3.0 \leq \log(n_{\text{H}}/\text{cm}^{-3}) \leq 0$ in steps of 0.10 dex, as we describe above in Section 7.3.1.

We looked to estimate the metallicity based on O I as this element depletes very little in warm ionized gas and has a negligible ionization correction for clouds with $\log(N_{\text{HI}}/\text{cm}^{-2}) \geq 19$ due to charge exchange between hydrogen and oxygen (S. M. Viegas 1995), which is consistent with what we found in our photoionization models (see Figures 17 and 18). However, given the FUSE resolution of 20 km s^{-1} , we cannot rule out that the O I 1039 Å component at $v_{\text{LSR}} = +120 \text{ km s}^{-1}$ may be saturated, therefore we give a limit on $[\text{O I}/\text{H I}] \geq -0.67$. Additionally, adopting the O I column density as it is from the profile fitting results in nonphysical outcomes from the photoionization modeling. Fortunately, we have a good unsaturated measurement for S II which yields a sulfur ion abundance of $[\text{S II}/\text{H I}] = +0.24 \pm 0.11$. Sulfur is also known to deplete very little onto dust, but does require an ionization correction to the ion abundance to account for the amount of sulfur present in other ion stages. J. A. Collins et al. (2003) conducted a study to determine the range of ionization corrections for S II as a function of $\log N_{\text{HI}}$ in different density regimes, where the highest and lowest ionization corrections corresponding to our H I column densities range between $-0.7 \lesssim \text{IC}_{\text{S II}} \lesssim -0.3$, respectively. This range of correction values could result in an elemental abundance for $[\text{S}/\text{H}]$ from approximately -0.5 to nearly solar, therefore we permitted the optimize model to vary over a larger range of metallicity values to fully explore the effect of metallicity on the model column densities. We chose a range from -0.76 to $+0.06$ in steps of 0.10 dex, which conservatively contains within it both the observed $[\text{O I}/\text{H I}]$ lower limit and the possibility of a solar abundance.

The results of the optimization model describe a mostly ionized cloud with a hydrogen ionization fraction of $\chi_{\text{H II}} = 0.97$ and $\log(T/\text{K}) \approx 4$. The optimal hydrogen number density and hydrogen-ionizing photon flux are $\log(n_{\text{H}}/\text{cm}^{-3}) = -2.13$ and

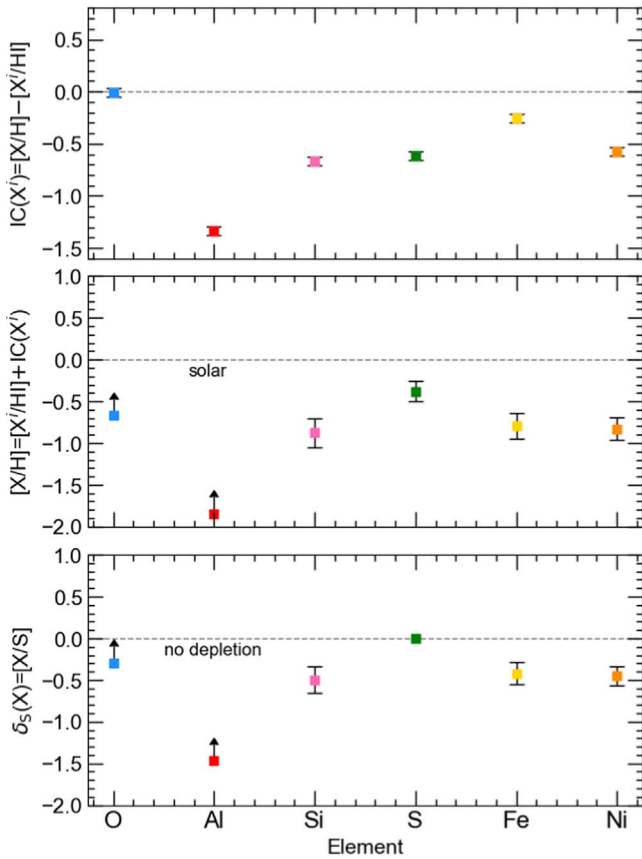


Figure 18. Photoionization modeling results for the $v_{\text{LSR}} \approx +120 \text{ km s}^{-1}$ component toward Sk - 69°175 with optimal hydrogen number density $\log(n_{\text{H}}/\text{cm}^{-3}) = -2.13$ and hydrogen-ionizing photon flux of $\log(\Phi_{\text{H}}/\text{photons cm}^{-2} \text{ s}^{-1}) = 5.85$. Top panel: ionization corrections for the six low ions (O I, Al II, Si II, S II, Fe II, and Ni II). The gray horizontal line at zero marks no ionization correction. Middle panel: comparison of the ionization-corrected elemental abundances. The gray dashed horizontal line marks solar abundance. Bottom panel: comparison of the levels of depletion among different elements $\delta_{\text{S}}(X) = [X/S]$. The gray horizontal line marks no depletion of the element relative to sulfur, assuming a solar abundance.

$\log(\Phi_{\text{H}}/\text{photons cm}^{-2} \text{ s}^{-1}) = 5.85$, respectively. The characteristic thickness of the absorbing neutral gas layer is 0.67 kpc, calculated from the hydrogen number density and the neutral gas column density, i.e., $r = N_{\text{HI}}/n_{\text{H}}$. Since this component is seen somewhere along the line of sight to Sk - 69°175 in the LMC, exposure to this ionizing photon flux places the receding cloud at a radial distance of either 3.6 kpc from the center of the LMC or 6.6 kpc from our position in the disk of the MW.

We find an ionization correction of $\text{IC}(\text{S}) = -0.62 \text{ dex}$ and a gas-phase element abundance of $[\text{S}/\text{H}] = -0.38 \pm 0.12$. This is consistent with the lower limit to the gas-phase oxygen element abundance $[\text{O}/\text{H}] \geq -0.67$. We calculate ionization-corrected gas-phase abundances of $[\text{Al}/\text{H}] \geq -1.85$, $[\text{Si}/\text{H}] = -0.88 \pm 0.18$, $[\text{Fe}/\text{H}] = -0.80 \pm 0.15$, and $[\text{Ni}/\text{H}] = -0.83 \pm 0.13$ (see Table 9 and the top and middle panels of Figure 18). We also checked for UV dust depletion effects in this component using the same procedure described above in Section 7.3.1. In this case, we calculate the depletion of the refractory elements relative to the unsaturated volatile element sulfur. For this component, we find evidence of moderate dust depletion for silicon, iron, and nickel of $\delta_{\text{S}}(\text{Si}) = -0.50 \pm 0.16$, $\delta_{\text{S}}(\text{Fe}) = -0.42 \pm 0.13$, and $\delta_{\text{S}}(\text{Ni}) = -0.45 \pm 0.11$.

Overall, these physical characteristics (i.e., mostly photo-ionized, warm, subsolar metallicity, moderate dust depletion)

Table 9
Summary of Photoionization Modeling Results for $v_{\text{LSR}} \approx +120 \text{ km s}^{-1}$
Component toward Sk - 69°175

Element (X)	$\text{IC}(X')$	$[\text{X}/\text{H}]$	$\delta_{\text{S}}(X)$
O	-0.01 ± 0.04	≥ -0.67	≥ -0.29
Al	-1.34 ± 0.04	≥ -1.85	≥ -1.47
Si	-0.67 ± 0.04	-0.88 ± 0.18	-0.50 ± 0.16
S	-0.62 ± 0.04	-0.38 ± 0.12	...
Fe	-0.26 ± 0.04	-0.80 ± 0.15	-0.42 ± 0.13
Ni	-0.58 ± 0.04	-0.83 ± 0.13	-0.45 ± 0.11

suggest the cloud seen near $+120 \text{ km s}^{-1}$ originates from a galactic disk. We note that the subsolar element abundance $[\text{S}/\text{H}] = -0.38 \pm 0.12$ ($42^{+13}_{-10}\%$ solar) is consistent with the current-day metallicity of the LMC of 46% (S. C. Russell & M. A. Dopita 1992). For the cloud to have originated from the MW Galactic disk, we expect that the cloud should have a solar or supersolar metallicity unless the cloud has undergone significant mixing (J. A. Gritton et al. 2014) over the predicted distance from the MW of 6.6 kpc.

8. Galaxy Simulation

To aid in the interpretation of our observations, we incorporate high-resolution hydrodynamic simulations of the LMC, SMC, and MW galaxies. These GIZMO simulations utilized a “meshless finite-mass” hydrodynamics scheme (V. Springel 2005; P. F. Hopkins 2015). These simulated galaxies consist of live dark matter halos that include coronal gas at their respective virial temperatures. The LMC and SMC have stellar and gaseous disks that are in agreement with observations and follow the orbital history of the Magellanic Clouds. This simulation follows the V. Springel & L. Hernquist (2003) star formation, mechanical stellar feedback, and the R. P. C. Wiersma et al. (2009) and P. F. Hopkins et al. (2018) metal-dependent heating and cooling prescriptions. We outline the details of these simulations in S. Lucchini et al. (2024).

Our simulation produces a starburst region that is similar to 30 Doradus, but one that has a less active history. This simulated region formed $1.3 \times 10^5 M_{\odot}$ of stars in the past 2 Myr and $2.4 \times 10^5 M_{\odot}$ within the past 20 Myr. We include snapshots of the low- and high-ion gas distribution of the simulated 30 Doradus analog at the present day and 20 Myr in the future in Figure 19. Due to the high present-day star formation rate, a large ($\sim 1 \text{ kpc}$ in diameter) bubble in the ISM forms in 20 Myr as a consequence of the supernovae feedback. The present-day morphology of the low-ionization species in this simulation is similar to that of the H I gas distribution of 30 Doradus (see Figure 1), where the star formation activity is being fed by high-column-density gas that is surrounded by pockets of relatively lower-column-density gas in which ejected material can more easily traverse.

As the LMC and SMC approach the MW, the LMC’s coronal gas and wind interact with the MW’s halo, and they become distorted due to a combination of ram pressure and tidal forces. We include a schematic of the resultant geometry of the mangled Magellanic Corona (S. Lucchini et al. 2020, 2021) relative to the MW and SMC in Figure 20. The present-day warped Magellanic Corona is shaded orange and the MW’s coronal gas is depicted in purple. The arrows in blue emanating from the LMC’s disk represent the LMC’s galactic wind, which is encapsulated within the Magellanic Corona. While the Magellanic Corona is

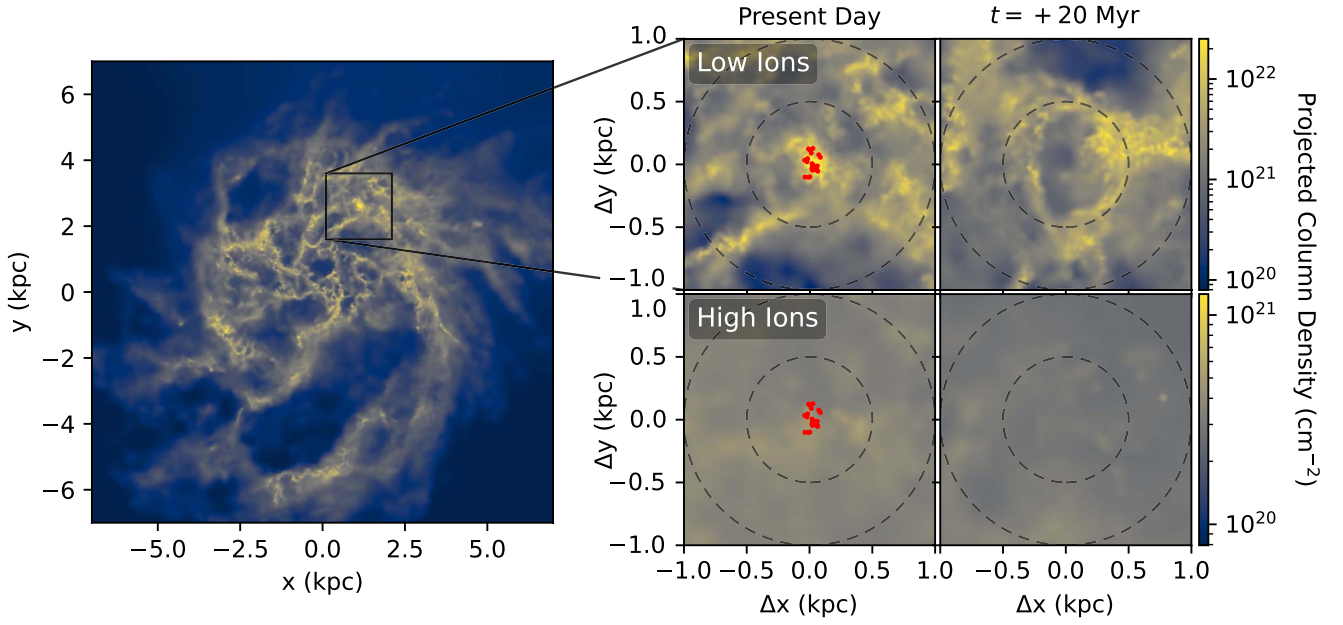


Figure 19. Face-on projection of the simulated LMC highlighting the 30 Doradus analog region. Color bars represent projected column density in cm^{-2} . The left panel depicts the entire face of the LMC disk, with the four panels on the right showing a zoomed-in region around the 30 Doradus analog. Of the four panels on the right, the top two panels highlight the distribution of H I corresponding to the low ions, and the bottom panels highlight the H II corresponding to the high ions. The left two panels feature the gas at the present day, having formed $1.2 \times 10^3 M_\odot$ of stars within 2 Myr, and the right panels emphasize the appearance of the region at 20 Myr of evolution. A supernova bubble is visible extending ~ 1 kpc in diameter. The gray dashed lines mark circles with radii of 0.5 and 1 kpc as in Figure 1.

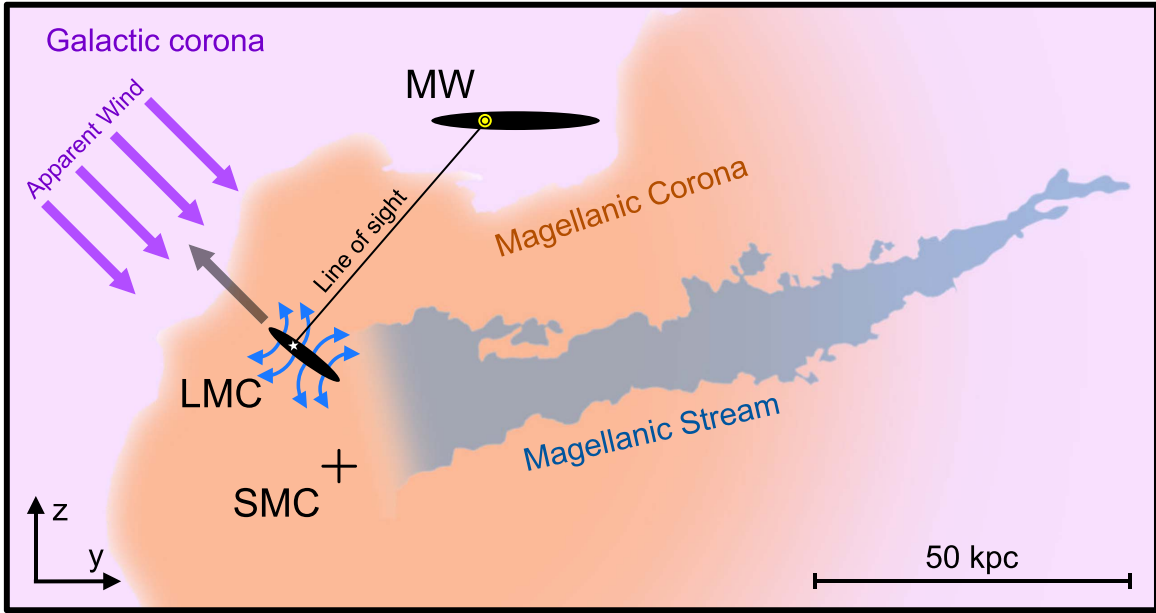


Figure 20. Schematic of the present-day, warped Magellanic Corona (in orange) in the y - z plane and the predicted position of the Magellanic Stream (in blue; S. Lucchini et al. 2020, 2021). The present-day LMC velocity is indicated with a gray arrow and the opposing direction of the apparent wind through the MW's coronal gas (in purple) is marked with purple arrows. The blue arrows that emanate from the LMC's disk represent the LMC's galactic wind, which is encased within the Magellanic Corona. The black line that extends between the Sun and a star embedded within the LMC's disk illustrates the line of sight that we are able to probe in this absorption-line study.

significantly warped from its initially spherical shape, it still surrounds the Clouds today and may shield the LMC's wind from the ram pressure effects associated with the MW's gaseous halo.

9. Discussion

Below, we discuss the origin of the wind in detail and compare our findings with the existing literature on 30 Doradus and the global LMC wind in general. As previously detailed in Section 5, our analysis of the radial distribution of the

blueshifted gas in the foreground to 30 Doradus, with velocities reaching up to $v_{\text{LSR}} \approx +150 \text{ km s}^{-1}$, suggests that this material is primarily associated with the galactic wind driven by 30 Doradus. However, additional evidence—such as the relationship between cloud speed and column density described in Section 5.2, trends in ion ratios, and insights from photoionization modeling—indicates that some of the absorption within the range $+100 \lesssim v_{\text{LSR}} \lesssim +150 \text{ km s}^{-1}$ may also be attributed to the LMC wind, along with contributions from the

MW's HVCs. In particular, the highest wind speeds based on our lighter cloud assumption, as discussed in Section 5.2, are observed along the first four sightlines, which are located near the most highly ionized central region of 30 Doradus, where the massive star cluster R136 resides (see N. R. Walborn 1991; N. Castro et al. 2018 and references therein). Given the extreme conditions in this region, the presence of concentrated, high-velocity outflows along these sightlines is expected.

We estimate the outflow mass and the outflow rate from the low ions for the 30 Doradus region encompassing these inner four sightlines that lie out to a projected radial distance of $R = 0.45$ kpc from the center of 30 Doradus. For this, we utilize the average Si II AOD column density of $\log(N_{\text{SiII}}/\text{cm}^{-2}) \approx 15.36$ for the sightlines Sk $-69^{\circ}246$ and Sk $-68^{\circ}135$ integrated in the velocity range of $+100 \text{ km s}^{-1} < v_{\text{LSR}} < \text{LMC's disk boundary}$. Both of these sightlines have Si II $\lambda 1808$ measurements available which offer unsaturated column densities. The total column density measured this way is also consistent with the results from the Voigt profile fitting. The outflowing mass (M_{outflow}) is directly proportional to the product of the column density of the ion (N) and the surface area of the outflow (A):

$$M_{\text{outflow}} = \mu \langle N_{\text{H}} \rangle A \cos i, \quad (8)$$

where we multiply by a factor of $\cos i$ to account for the LMC's inclination angle of $i \approx 23.4^{\circ}$ (Y. Choi et al. 2022) and we adopt an average particle mass of $\mu = 1.3m_p$. The surface area of the outflow can be written as $A = c_f \pi R^2$, where we consider a covering fraction of $c_f = 1.0$ for the low-ionization species as this region of 30 Doradus remains active across its entire area and we detect the outflows in all the sightlines we studied. Assuming the metallicity of the LMC ($Z = 0.5 Z_{\odot}$) from S. C. Russell & M. A. Dopita (1992), the mass equation for the nearside outflow can be written as follows (see K. A. Barger et al. 2016):

$$M_{\text{outflow}} = \frac{1.3m_p \langle N_{\text{SiII}} \rangle \pi R^2 \cos i}{Z/Z_{\odot} (\text{Si}/\text{H})_{\odot}}. \quad (9)$$

We estimate a low-ion probed baryon mass outflow of $M_{\text{baryon}} \approx 8.6 \times 10^5 M_{\odot}$ within 0.5 of 30 Doradus. If we restrict the maximum wind speed to $v_{\text{LSR}} = 150 \text{ km s}^{-1}$ instead of $v_{\text{LSR}} = 100 \text{ km s}^{-1}$, the average Si II AOD column density will only decrease by -0.06 dex to a value of $\log(N_{\text{SiII}}/\text{cm}^{-2}) \approx 15.29$, which does not result in any significant reduction in the outflow mass. Based on the discussion in Section 3.3, extending the LMC disk width by $\sim 10 \text{ km s}^{-1}$ in the blueshifted direction would reduce the total average column density to $\log(N_{\text{SiII}}/\text{cm}^{-2}) \approx 15.18$ and the corresponding outflow mass would be $M_{\text{baryon}} \approx 5.7 \times 10^5 M_{\odot}$. Comparing with the outflow mass estimated by K. A. Barger et al. (2016), 30 Doradus alone is found to be contributing a significant fraction of the total outflowing low ions from the entire LMC.

Considering the oldest star cluster, the age of 30 Doradus has been determined to be between 26.5 and 31.5 Myr old (M. Cignoni et al. 2016). Studies also indicate that the rate of star formation in the 30 Doradus region surpassed the average rate in the LMC around 20 Myr ago (M. Cignoni et al. 2015). Assuming an average line-of-sight speed of $100 \leq \langle |v| \rangle \leq 150 \text{ km s}^{-1}$, the wind originating from 30 Doradus could have traveled a distance 2–4.6 kpc over the time period of 20–30 Myr. Remarkably, this distance range aligns with one of the solutions obtained from photoionization modeling for a component at $v_{\text{LSR}} = +120 \text{ km s}^{-1}$ toward Sk $-69^{\circ}175$. This particular component is found to be at a radial

distance of 3.6 kpc from the LMC, consistent with the observation. Moreover, assuming a maximum outflow timescale of $t_{\text{outflow}} = 31.5$ Myr based on the oldest star cluster in 30 Doradus (M. Cignoni et al. 2016), the outflow rate would be $\dot{M}_{\text{outflow}} \gtrsim 0.02 M_{\odot} \text{ yr}^{-1}$. Comparing our measurement for the outflow mass rate with the star formation rate of the 30 Doradus region ($\text{SFR} = 0.18 M_{\odot} \text{ yr}^{-1}$; O. Nayak et al. 2023), we estimate a mass loading factor of $\eta \gtrsim 0.10$. Additionally, we also estimate the outflow rate using the cloud velocity and column density relation from T. M. Heckman (2002; see Appendix B) and based on our previous assumption of the lighter cloud hypothesis discussed in Section 5.2. Assuming a 30 Doradus starburst radius of 0.15 kpc (L. A. Lopez et al. 2011) and an LMC metallicity of $Z = 0.5 Z_{\odot}$, we calculate an outflow rate of $\dot{M}_{\text{outflow}} = 0.026 \pm 0.003 M_{\odot} \text{ yr}^{-1}$, consistent with the outflow rate obtained from the conservative approach discussed above.

Our findings are in alignment with the results reported by D. A. Ciampa et al. (2021) based on an $\text{H}\alpha$ emission map of the LMC. They observed that the 30 Doradus region generates winds with significantly higher speeds, surpassing a velocity of $v_{\text{LMCSR}} > -175 \text{ km s}^{-1}$, in contrast to the more general galactic winds, which exhibit velocities around $v_{\text{LMCSR}} < -110 \text{ km s}^{-1}$. Additionally, D. A. Ciampa et al. (2021) noted an asymmetry in the morphology of the $\text{H}\alpha$ emission associated with the global wind, where the wind is notably more concentrated in the quadrant of the galaxy that encompasses 30 Doradus. Based on high-resolution emission data of [O III] from the 30 Doradus region, M. P. Redman et al. (2003) also reported a wind velocity that closely matched the velocities observed in the fast-moving components in our work.

Previously reported in the study by N. Lehner et al. (2009), there is evidence of higher concentrations of HVCs in the vicinity of the 30 Doradus region based on the gradient in the average velocities of HVCs observed across the entire expanse of the LMC. Similarly, S. Kim et al. (1999) suggested a higher density of supergiant shells closer to the 30 Doradus region. These HVCs near 30 Doradus may be linked with H I voids that have been generated by explosive stellar events, including supernova explosions. Indeed, L. Staveley-Smith et al. (2003) found a connection between the formation of H I voids in the LMC's disk and supergiant shells (see their Figures 10 and 11) as a consequence of such explosive events.

We also compare the ionization properties of the winds between the 30 Doradus region and the entire LMC by examining the average [Si II/O I]. To facilitate the comparison, we contrasted our values with the results presented in N. Lehner et al. (2009), which specifically investigated the HVCs directed toward the LMC within the velocity range of $+90 \lesssim v_{\text{LSR}} \lesssim +175 \text{ km s}^{-1}$. Although we find wind speeds reaching up to $v_{\text{LSR}} \approx +215 \text{ km s}^{-1}$, we focus solely on the wind components in the range of $+90 \lesssim v_{\text{LSR}} \lesssim +175 \text{ km s}^{-1}$ to match with the observations in N. Lehner et al. (2009) for comparison. Our findings for the 30 Doradus region reveal an average [Si II/O I] ratio of 0.69 dex with a dispersion of 0.29 dex, compared to the average ratio of 0.48 dex with a similar dispersion reported by N. Lehner et al. (2009). This relatively higher value observed in the 30 Doradus region is in line with expectations, as it is a result of the elevated radiation levels arising from the intense stellar activity in the area. In contrast, the average value for the entire LMC represents a mixture of active and passive regions, which naturally yields a lower average [Si II/O I] ratio.

While there is substantial evidence supporting the notion that the fast-moving winds originate from the intense stellar activities within

the 30 Doradus region, it is important to explore the other possibilities, such as the potential influence of the thick disk's motion and the gas dynamics resulting from tidal interactions. Typically, a galaxy's thick disk plays a dominant role in the overall rotational dynamics of the galaxy, and may exhibit some lag compared to the less dense thin disk (G. H. Heald et al. 2007; P. Kamphuis et al. 2007; T. Oosterloo et al. 2007). However, given the LMC's nearly face-on orientation ($i \approx 23.4^\circ$; Y. Choi et al. 2022), we may not be sensitive to absorption resulting from the thick disk's lag, as such effects are typically more pronounced in edge-on galaxies (see K. A. Barger et al. 2016 for details). Another plausible source of influence is the gravitational interactions between the Magellanic Clouds, which have given rise to various structures, including the Leading Arm, Magellanic Bridge, and Magellanic Stream (K. A. Barger et al. 2013; A. J. Fox et al. 2014). While the Leading Arm and Magellanic Bridge are situated relatively farther away from the 30 Doradus region, the proximity of the Magellanic Stream to this area warrants consideration. D. L. Nidever et al. (2008) traced one of the two filamentary structures in the Magellanic Stream back to the quadrant of the LMC that contains 30 Doradus. P. Richter et al. (2013) later found that this filament also has a metallicity consistent with an LMC origin. Nonetheless, our choice of sightlines on the opposite side of 30 Doradus to where that filament passes was deliberate, with intentions of avoiding material from this structure.

Considering that some studies propose the association of HVCs toward the LMC at a velocity of $+90 \lesssim v_{\text{LSR}} \lesssim +150 \text{ km s}^{-1}$ with the MW halo, rather than the LMC, as discussed in Section 3.4 (B. D. Savage & K. S. de Boer 1981; K. S. de Boer et al. 1990; P. Richter et al. 1999, 2015), it is crucial to explore these possibilities in the context of the 30 Doradus region. In particular, P. Richter et al. (2015) indicates that high-velocity absorption is identified in the spectrum of a MW halo star located at $d_\odot \lesssim 13.3 \text{ kpc}$ away or within 5.6 kpc from the Galactic disk, strongly indicating an association with the MW rather than the LMC for this absorber in this direction. However, our sightlines are specifically positioned either in the immediate core of 30 Doradus or in its close vicinity. The background halo star used by P. Richter et al. (2015) lies in the opposite side of 30 Doradus and outside the H I contour of the LMC disk based on the H I emission channel maps from D. A. Ciampa et al. (2021); the fast-moving absorber along this sightline may not represent the outflows from the LMC and could instead be associated with an HVC that lies in the foreground of the LMC.

We further explore the origin and properties of the absorption at $+100 \lesssim v_{\text{LSR}} \lesssim +150 \text{ km s}^{-1}$ using photoionization modeling available for two high-velocity components along two sightlines located at an offset angle $\gtrsim 0.65$ from the center of 30 Doradus. Photoionization modeling for the $v_{\text{LSR}} = +120 \text{ km s}^{-1}$ absorber toward Sk $- 69^\circ 175$ and the $v_{\text{LSR}} = +115 \text{ km s}^{-1}$ absorber toward BI 173 provides some insights into the dust depletion and the metallicity, which may be traced back to a specific origin of these absorbers. For the component toward BI 173, we find evidence of no dust depletion, with it being mostly neutral, cool, and with a lower metallicity of about -0.7 dex (see Section 7.3.1). For the component toward Sk $- 69^\circ 175$, we find evidence of moderate dust depletion and a subsolar metallicity of $[\text{S}/\text{H}] = -0.38 \pm 0.12$ (see Section 7.3.2), which is consistent with the current-day metallicity of the LMC (S. C. Russell & M. A. Dopita 1992).

However, there are several detections of dust depletion in MW HVCs too, typically with low to moderate levels. The $\delta(\text{Si}) = -0.50 \pm 0.16$, $\delta(\text{Fe}) = -0.42 \pm 0.13$, and

$\delta(\text{Ni}) = -0.45 \pm 0.11 \text{ dex}$ depletion patterns that we measure for the absorber along the Sk $- 69^\circ 175$ sightline are very similar to what A. J. Fox et al. (2023) found for HVC Complex C at $\delta(\text{Si}) \approx -0.29$, $\delta(\text{Fe}) \approx -0.42$, and $\delta(\text{Al}) \approx -0.53 \text{ dex}$. For an HVC in the inner galaxy, F. H. Cashman et al. (2023) reported a value of $[\text{Fe}/\text{O}] = -0.3 \pm 0.20 \text{ dex}$, suggesting moderate dust depletion. While a metallicity of $[\text{S}/\text{H}] = -0.38 \pm 0.12$ for the $v_{\text{LSR}} = +120 \text{ km s}^{-1}$ component toward Sk $- 69^\circ 175$ is close to the LMC metallicity, it is also close to several MW HVCs, such as the Smith Cloud of $[\text{S}/\text{H}] = -0.28 \pm 0.14 \text{ dex}$ (A. J. Fox et al. 2016) and Complex C of $[\text{S}/\text{H}] = -0.51 \pm 0.16 \text{ dex}$ (A. J. Fox et al. 2023). However, the speed of the cloud at $|v| \approx 145 \text{ km s}^{-1}$ relative to the LMC, the metallicity which agrees with that of the present-day LMC, the dust depletion being consistent with a galactic origin, and the alignment with the bursty 30 Doradus region makes this absorber more likely to be associated with the LMC wind than with the MW. In contrast, the high-velocity absorber along the BI 173 sightline with a lower metallicity and no signs of dust suggest that this material is more likely a MW HVC. Therefore, the high-velocity gas at $+90 \lesssim v_{\text{LSR}} \lesssim +150 \text{ km s}^{-1}$ along the four outer sightlines may represent a combination of both foreground MW HVCs and LMC wind.

As we observe significant outflows from 30 Doradus, questions arise about how these outflows withstand the direct headwind as the LMC orbits through the MW's gaseous halo. Studies have determined that this headwind directly impacts the leading edge of the LMC, resulting in the suppression of outflows on the nearside, while the effect is milder on the farside (C. Bustard et al. 2020; D. A. Ciampa et al. 2021). However, these studies did not consider the existence of the Magellanic Corona, which has been recently discovered both in observations (D. Krishnarao et al. 2022) and in simulations (S. Lucchini et al. 2020, 2021). From the galactic simulation, discussed in Section 8, although the Magellanic Corona has deviated significantly from its initially spherical shape, it still envelops the Magellanic Clouds today, providing shielding from the ram pressure effects of the MW's gaseous halo (see Figure 20). Furthermore, recent studies utilizing hydrodynamical simulations of the LMC (D. J. Setton et al. 2023) have suggested that the LMC's motion may generate a bow shock ahead of it, which could also help mitigate the effects of the ram pressure (see also Y. Zheng et al. 2024). K. A. Barger et al. (2016), utilizing a quasar as a background source to investigate the outflows from the LMC, observed symmetrical absorption on both the near and farsides, indicating that nearside outflows are not significantly suppressed. This also supports our speculation that there must be a protective mechanism against ram pressure affecting these outflows. Since the LMC might be on its first infall to the MW (G. Besla et al. 2007) and has a high velocity (N. Kallivayalil et al. 2013), both the bow shock and Magellanic Corona play an important role in protecting the LMC's disk from the MW's circumgalactic gas.

10. Summary

We investigate the absorption features along eight sightlines located within 1.7° of 30 Doradus. We intentionally chose sightlines residing on one side of 30 Doradus to avoid potential interference from Magellanic tidal structures, such as the Magellanic Stream. Our study combines UV absorption-line observations obtained with HST/STIS E140M and E230M gratings and FUSE, focusing on early-type stars in the LMC. Additionally, we complement our observations with ancillary H I 21 cm radio emission-line GASS and GASKAP observations associated with the LMC. Our primary findings are as follows:

1. *Origin and distribution of the gas.* The blueshifted gas in the foreground of 30 Doradus, with speeds up to $v_{\text{LSR}} = +150 \text{ km s}^{-1}$, is most likely associated with the galactic wind originating from 30 Doradus, based on its radial distribution (see Section 5.1). However, several results—for example, those based on the cloud speed versus column density relation (Section 5.2), trends in ion ratios (Section 7.1), and photoionization modeling (Section 7.3), in addition to those from other studies—suggest that some of the $+100 \lesssim v_{\text{LSR}} \lesssim +150 \text{ km s}^{-1}$ absorption might also belong to the LMC wind in addition to the MW HVCs.
2. *Outflow mass and outflow rate.* The integrated low-ion column densities across all wind velocities suggest a greater concentration of outflowing gas in the direction of 30 Doradus that gradually declines with the projected distance from the center of this starburst region. We estimate a low-ion probed baryon mass outflow of $M_{\text{outflow}} \approx (5.7\text{--}8.6) \times 10^5 M_{\odot}$ from within 0.52 of 30 Doradus. We further estimate a lower limit for the outflow rate to be $\dot{M}_{\text{outflow}} \gtrsim 0.02 M_{\odot} \text{ yr}^{-1}$ and a mass loading factor of $\eta \gtrsim 0.10$. We find that the outflows from this region contribute a significant fraction of the total low-ion outflow mass from the entire LMC.
3. *Ionization.* The observed ion ratios together with the photoionization modeling reveal that the wind components are multiphased, with the hydrogen ionization fraction ranging from 40% to 97%. We observe both spatial and kinematic variations in these ionization fractions. The typical smaller average b -values and an absence of significant offsets in the velocity centroids between O I and Si II suggest that the gas probed by the low ions is photoionized. For the high ions, the Si IV and C IV components are broader and kinematically offset from the low ions, suggesting that they are susceptible to collisions and are largely consistent with TMLs that exist in the wind.
4. *Metallicity and dust depletion.* Our photoionization modeling reveals the properties for two absorbers that lie at (i) $v_{\text{LSR}} \approx +120 \text{ km s}^{-1}$ toward Sk $- 69^{\circ}175$, and (ii) $v_{\text{LSR}} \approx +115 \text{ km s}^{-1}$ toward BI 173. We find evidence for moderate dust depletion for silicon, iron, and nickel of $\delta_{\text{S}}(\text{Si}) = -0.50 \pm 0.16$, $\delta_{\text{S}}(\text{Fe}) = -0.42 \pm 0.13$, and $\delta_{\text{S}}(\text{Ni}) = -0.45 \pm 0.11 \text{ dex}$ for the absorber along the Sk $- 69^{\circ}175$ sightline. This cloud also has a subsolar element abundance of $[\text{S}/\text{H}] = -0.38 \pm 0.12$, which is consistent with the current-day metallicity of the LMC. However, for the cloud toward BI 173, we find no evidence of dust ($\delta_{\text{O}}(\text{Fe}) = -0.02 \pm 0.11 \text{ dex}$) and a lower metallicity ($[\text{O}/\text{H}] = -0.70 \pm 0.13 \text{ dex}$). The mostly neutral, cool, low-metallicity, and dust-free properties suggest that the cloud seen near $v_{\text{LSR}} = +115 \text{ km s}^{-1}$ is a MW halo HVC.

Finally, our high-resolution hydrodynamical simulations of the LMC, SMC, and MW system using the GIZMO code suggest that the winds generated in our 30 Doradus-like region are only weakly affected by the direct headwind from the MW's halo. This is because the LMC's corona acts as a shield, protecting the outflows. Given that the LMC might be on its first infall to the MW (e.g., G. Besla et al. 2007) and moving at high velocity (e.g., N. Kallivayalil et al. 2013), both the bow shock and the Magellanic Corona play crucial roles in safeguarding the LMC's wind from the MW's circumgalactic gas.

This paper is the first in a series investigating the wind from the LMC, and future efforts will include a comprehensive analysis of its global wind patterns, its connection with the activity occurring within this galaxy, and the LMC's halo.

Acknowledgments

We sincerely thank the anonymous referee for their valuable feedback, which has significantly improved the quality of this paper. Support for this program was provided by NASA through the grant HST-AR-16602.001-A from the Space Telescope Science Institute, which is operated by the Association of Universities for Research in Astronomy, Inc. under NASA contract NAS5-26555. N.L. acknowledges support by NASA through grant Nos. HST-AR-16602 and HST-AR-17051 from the Space Telescope Science Institute. Additional support for A.H. was provided by NSF grant 2334434. This study used ULLYSES observations obtained with the NASA/ESA Hubble Space Telescope (J. Roman-Duval et al. 2020), retrieved from the Mikulski Archive for Space Telescopes (J. Roman-Duval 2020). STScI is operated by the Association of Universities for Research in Astronomy, Inc. under NASA contract NAS 5-26555. This work has made use of the Vienna Atomic Line Data Base (VALD) database, operated at Uppsala University, the Institute of Astronomy RAS in Moscow, and the University of Vienna. This scientific work uses data obtained from Inyarrimanha Ilgari Bundara/the Murchison Radio-astronomy Observatory. We acknowledge the Wajarri Yamaji People as the Traditional Owners and native title holders of the Observatory site. CSIRO's ASKAP radio telescope is part of the Australia Telescope National Facility (<https://ror.org/05qajvd42>). Operation of ASKAP is funded by the Australian Government with support from the National Collaborative Research Infrastructure Strategy. ASKAP uses the resources of the Pawsey Supercomputing Research Centre. Establishment of ASKAP, Inyarrimanha Ilgari Bundara, the CSIRO Murchison Radio-astronomy Observatory and the Pawsey Supercomputing Research Centre are initiatives of the Australian Government, with support from the Government of Western Australia and the Science and Industry Endowment Fund. GASKAP-HI is partially funded by the Australian Government through an Australian Research Council Australian Laureate Fellowship (project number FL210100039 awarded to N.Mc-G). This study used archived HI LMC data obtained through https://www.astro.uni-bonn.de/hisurvey/AllSky_gauss/. All our data products are available at MAST as a High Level Science Product via doi:10.17909/fnra-7754.

Software: Astropy (Astropy Collaboration et al. 2013, 2018, 2022), Cloudy (G. J. Ferland et al. 2017), GIZMO (V. Springel 2005; P. F. Hopkins 2015), VoigtFit (J.-K. Krogager 2018), galrad (<https://github.com/Deech08/galrad>).

Appendix A Voigt Profile Fitting Results

We present the spectral plot stacks for all the sightlines analyzed in this study in Figure 21, except for sightline Sk $- 69^{\circ}246$, which was presented in Figure 5. These plot stacks are presented in increasing order of the angular separation of these sightlines from the center of 30 Doradus.

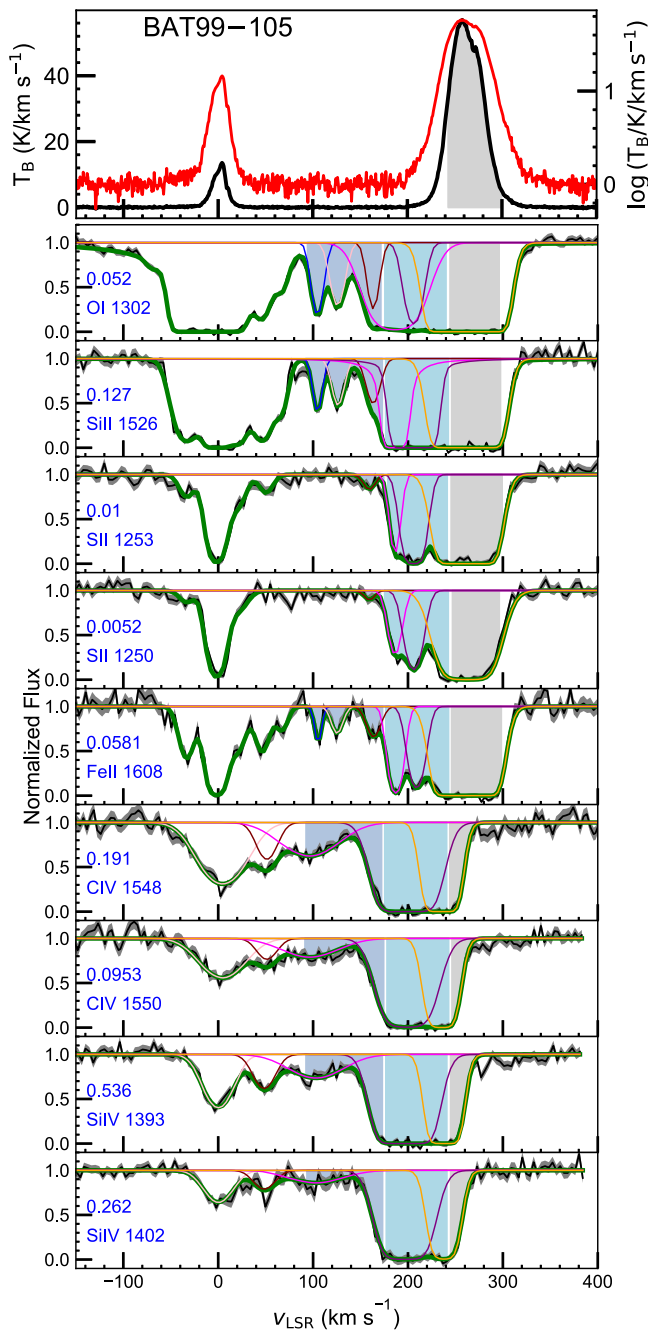


Figure 21. These plot stacks are the same as Figure 5 for sightline SK – 69° 246, but are for the remaining seven of the eight sightlines explored in this study.

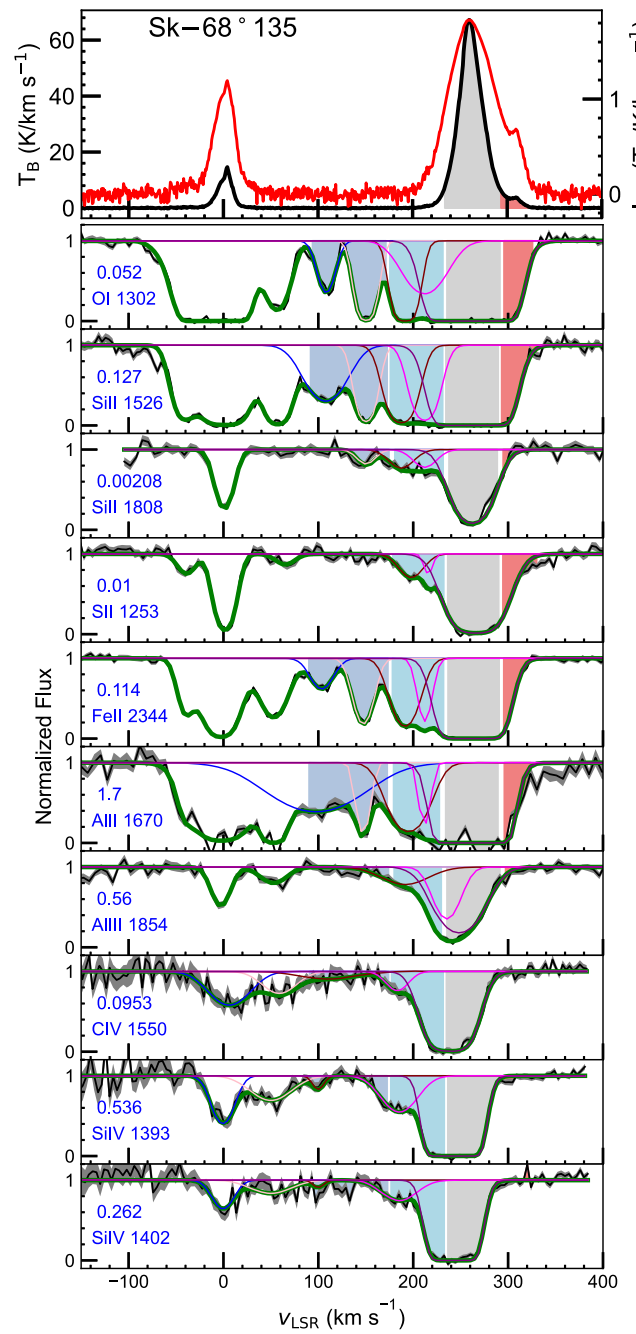


Figure 21. (Continued.)

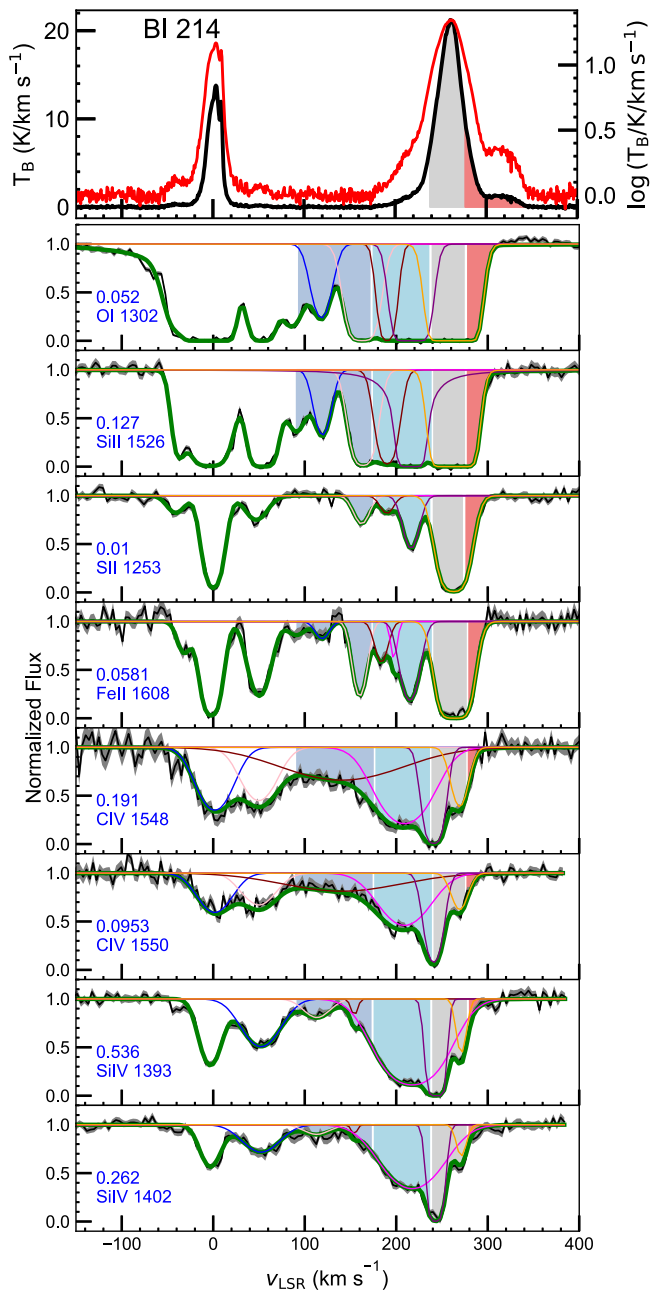


Figure 21. (Continued.)

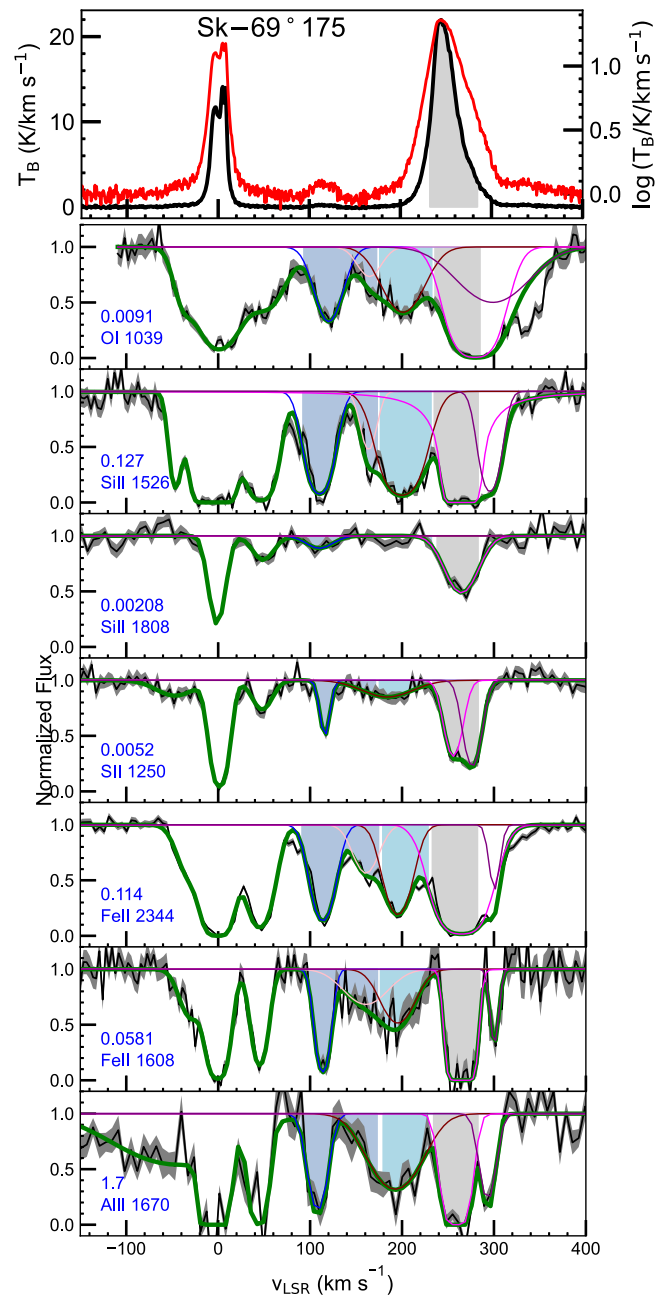


Figure 21. (Continued.)

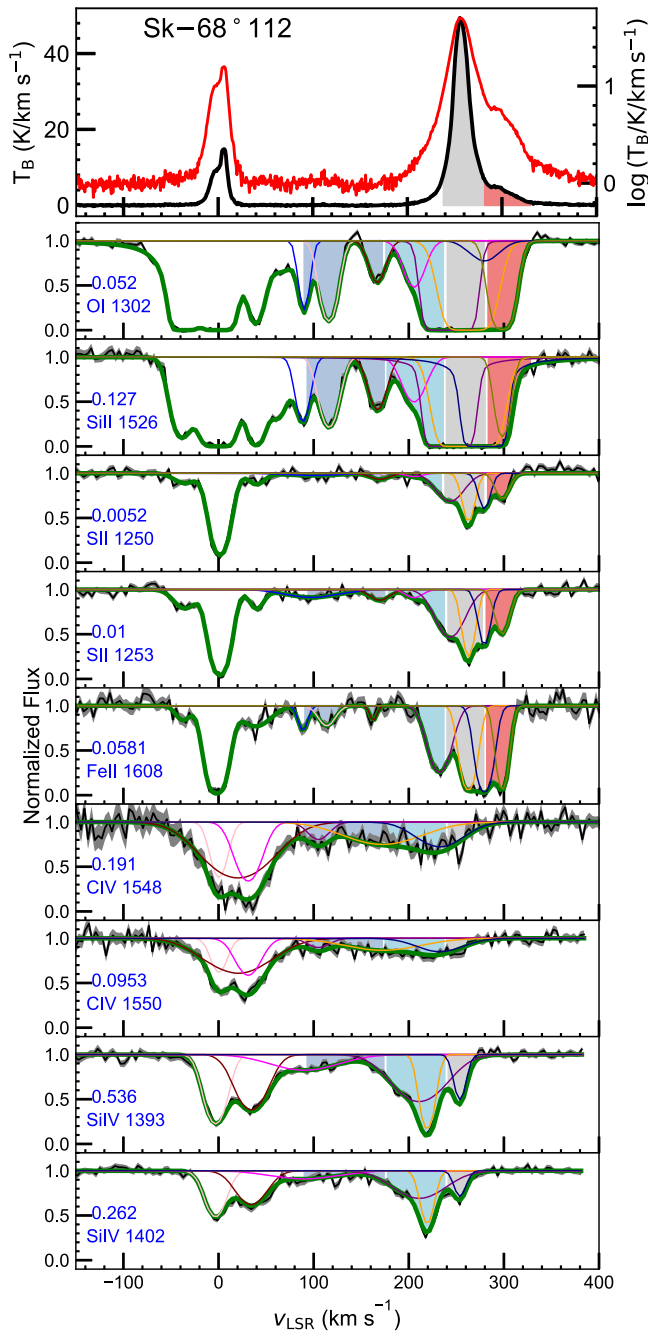


Figure 21. (Continued.)

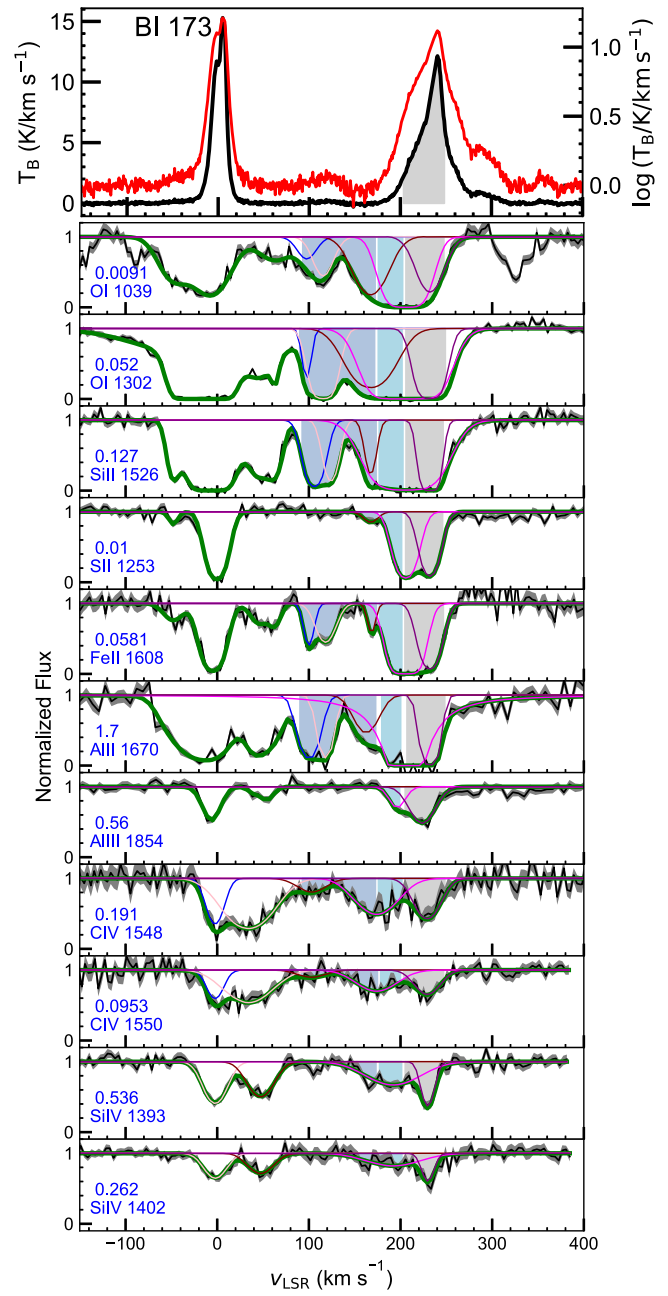


Figure 21. (Continued.)

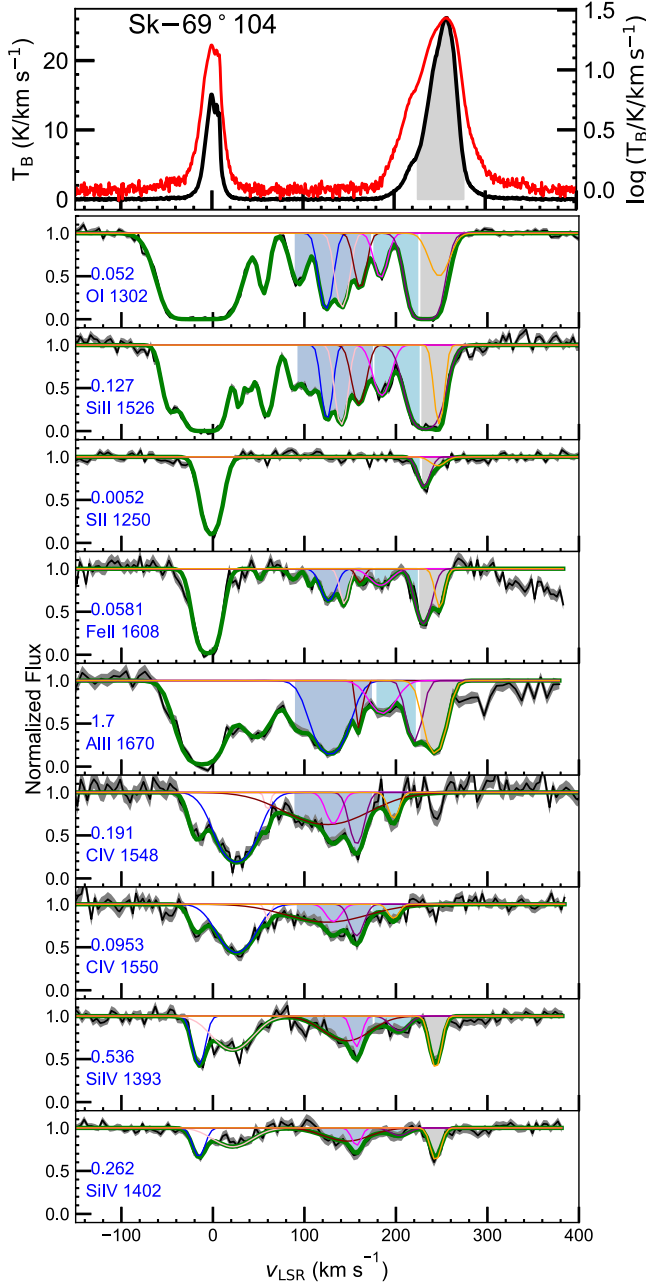


Figure 21. (Continued.)

Appendix B Column Density versus Velocity

The galactic wind model from T. M. Heckman (2002) describes starburst-driven, multiphase outflows powered by mechanical energy from supernovae and stellar winds. These winds expel interstellar material into galactic halos and beyond, with cloud velocities (v_{cloud}) determined by ram pressure acceleration:

$$v_{\text{cloud}} \sim 600 \dot{p}_{34}^{1/2} \Omega_w^{-1/2} r_0^{-1/2} N_{\text{cloud},21}^{-1/2} \text{ km s}^{-1}, \quad (\text{B1})$$

where \dot{p}_{34} represents the wind's momentum flux in units of 10^{34} dynes, Ω_w is the wind's solid angle, r_0 is considered to be the radius of the star-forming region in kiloparsec, and $N_{\text{cloud},21}$ is the cloud's column density in units of 10^{21} cm^{-2} . The inverse

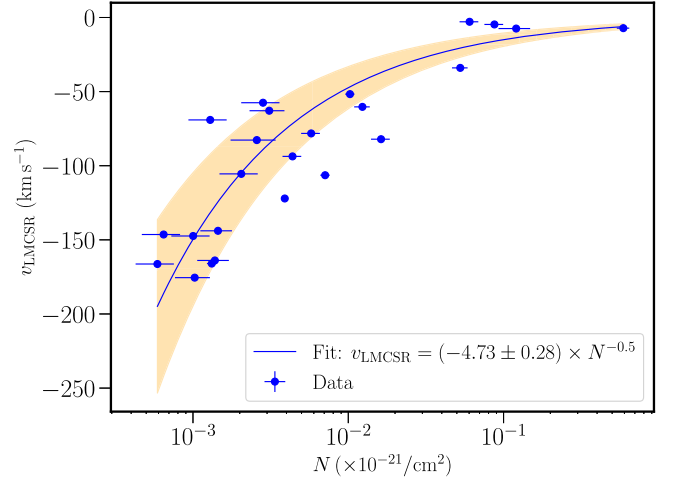


Figure 22. Neutral hydrogen column densities derived from the $N_{\text{Fe II}}$ column densities assuming an $Z = 0.5 Z_{\odot}$ abundance and no ionization correction. We only include Voigt-fitted column densities for the four nearest sightlines to 30 Doradus, with velocities extending to $v_{\text{LMCSR}} \approx -175 \text{ km s}^{-1}$. The blue trend line and the associated yellow 5σ uncertainty envelope represent a fit to the T. M. Heckman (2002) model, which describes the velocity trend of gas clouds that are accelerated by a starburst-driven galactic wind.

dependence of v_{cloud} on $N_{\text{cloud},21}$ implies that denser clouds accelerate more slowly. We explore the relationship between the speed of the cloud and component column density (see Figure 22) following this model and under our assumption that lower-column-density clouds move faster (see Section 5.2). We demonstrate that our data can be well fitted under this assumption, yielding an outflow mass rate comparable to our more conservative estimate (see Section 9).

Appendix C Doppler Parameters Distribution

We compare the magnitude of the b -values across the entire velocity range from the MW to the LMC using Fe II (see Figure 23). We selected Fe II because it offers multiple transitions (Fe II λ 1608, 2249, 2260, 2344), which aids in obtaining robust measurements for the line widths. Also, the combination of these lines has the advantage of providing a substantial number of detectable components without being too weak or too strong to saturate when compared to other ions. Furthermore, to ensure the reliability of the b -values, we retained those components that were significantly detected, specifically those with a FWHM greater than the instrumental profile.

To test whether or not the line widths in these kinematically different regions are drawn from the same underlying population, we used the Anderson–Darling statistical test. We found that there is no statistically significant differences in b -values among these regions at the 95% confidence level. We subdivide the galactic wind region further into two velocity regimes: (i) a fast-moving component ($+150 \lesssim v_{\text{LSR}} \lesssim +175 \text{ km s}^{-1}$), which exhibits a mean b -value ($10.1 \pm 9.7 \text{ km s}^{-1}$), and (ii) a slower-moving counterpart ($+175 \lesssim v_{\text{LSR}} \lesssim +210 \text{ km s}^{-1}$), which exhibits a larger mean b -value of $12.5 \pm 6.1 \text{ km s}^{-1}$. This small contrast in b -values between these groups may be attributed to the blending of weaker components within the slower-moving ones. Moreover, we also do not observe any specific trend in the magnitude of the b -values with respect to the angular distance from 30 Doradus. We discuss the line widths of both the low and

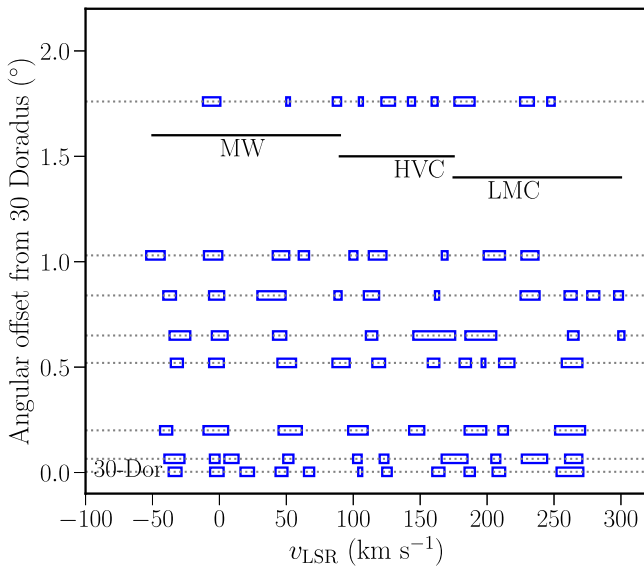


Figure 23. Comparison of Doppler b -values distribution across all eight sightlines at varying angular separations from 30 Doradus for Fe II lines covering the entire velocity range from the MW to the LMC. The widths of the rectangular boxes are equal to the magnitude of the Doppler b -value. The centers of these boxes represent the velocity centroids of the individual components. The horizontal dotted lines are drawn at the corresponding angular separations of these sightlines from the center of 30 Doradus. The three horizontal lines in black show the approximate velocity ranges for the MW, HVC, and the LMC regions.

high ions further in Section 6.1. Overall, we did not find a statistically significant difference in the mean b -values between any of these velocity subregions.

ORCID iDs

Suraj Poudel <https://orcid.org/0000-0003-0536-3081>
 Jo Vazquez <https://orcid.org/0000-0003-2308-8351>
 Kathleen A. Barger <https://orcid.org/0000-0001-5817-0932>
 Frances H. Cashman <https://orcid.org/0000-0003-4237-3553>
 Andrew J. Fox <https://orcid.org/0000-0003-0724-4115>
 Nicolas Lehner <https://orcid.org/0000-0001-9158-0829>
 Scott Lucchini <https://orcid.org/0000-0001-9982-0241>
 Dhanesh Krishnarao <https://orcid.org/0000-0002-7955-7359>
 N. M. McClure-Griffiths <https://orcid.org/0000-0003-2730-957X>
 Jason Tumlinson <https://orcid.org/0000-0002-7982-412X>
 Ananya Goon Tuli <https://orcid.org/0000-0001-6398-5466>
 Jacco Th. van Loon <https://orcid.org/0000-0002-1272-3017>
 Julia Roman-Duval <https://orcid.org/0000-0001-6326-7069>
 Yik Ki Ma <https://orcid.org/0000-0003-0742-2006>
 Callum Lynn <https://orcid.org/0000-0001-6846-5347>
 Min-Young Lee <https://orcid.org/0000-0002-9888-0784>
 Denis Leahy <https://orcid.org/0000-0002-4814-958X>

References

Asplund, M., Grevesse, N., Sauval, A. J., & Scott, P. 2009, *ARA&A*, **47**, 481
 Astropy Collaboration, Price-Whelan, A. M., Lim, P. L., et al. 2022, *ApJ*, **935**, 167
 Astropy Collaboration, Price-Whelan, A. M., Sipőcz, B. M., et al. 2018, *AJ*, **156**, 123

Astropy Collaboration, Robitaille, T. P., Tollerud, E. J., et al. 2013, *A&A*, **558**, A33
 Barger, K. A., Haffner, L. M., & Bland-Hawthorn, J. 2013, *ApJ*, **771**, 132
 Barger, K. A., Lehner, N., & Howk, J. C. 2016, *ApJ*, **817**, 91
 Besla, G., Kallivayalil, N., Hernquist, L., et al. 2007, *ApJ*, **668**, 949
 Bland-Hawthorn, J., & Maloney, P. R. 1999, *ApJL*, **510**, L33
 Bland-Hawthorn, J., Maloney, P. R., Sutherland, R., et al. 2019, *ApJ*, **886**, 45
 Bustard, C., Zweibel, E. G., D’Onghia, E., Gallagher, J. S. I., & Farber, R. 2020, *ApJ*, **893**, 29
 Cashman, F. H., Fox, A. J., Wakker, B. P., et al. 2023, *ApJ*, **944**, 65
 Cashman, F. H., Kulkarni, V. P., Kisieliński, R., Ferland, G. J., & Bogdanovich, P. 2017, *ApJS*, **230**, 8
 Castro, N., Crowther, P. A., Evans, C. J., et al. 2018, *A&A*, **614**, A147
 Chatzikos, M., Bianchi, S., Camilloni, F., et al. 2023, *RMxAA*, **59**, 327
 Choi, Y., Olsen, K. A. G., Besla, G., et al. 2022, *ApJ*, **927**, 153
 Ciampa, D. A., Barger, K. A., Lehner, N., et al. 2021, *ApJ*, **908**, 62
 Cignoni, M., Sabbi, E., van der Marel, R. P., et al. 2015, *ApJ*, **811**, 76
 Cignoni, M., Sabbi, E., van der Marel, R. P., et al. 2016, *ApJ*, **833**, 154
 Collins, J. A., Shull, J. M., & Giroux, M. L. 2003, *ApJ*, **585**, 336
 Danforth, C. W., Howk, J. C., Fullerton, A. W., Blair, W. P., & Sembach, K. R. 2002, *ApJS*, **139**, 81
 Davies, R. D., Buhl, D., & Jafolla, J. 1976, *A&AS*, **23**, 181
 de Boer, K. S., Morras, R., & Bajaja, E. 1990, *A&A*, **233**, 523
 De Cia, A., Roman-Duval, J., Konstantopoulou, C., et al. 2024, *A&A*, **683**, A216
 de Grijs, R., Wicker, J. E., & Bono, G. 2014, *AJ*, **147**, 122
 Dickey, J. M., McClure-Griffiths, N., Gibson, S. J., et al. 2013, *PASA*, **30**, e003
 D’Onghia, E., & Fox, A. J. 2016, *ARA&A*, **54**, 363
 Doran, E. I., Crowther, P. A., de Koter, A., et al. 2013, *A&A*, **558**, A134
 Ferland, G. J., Chatzikos, M., Guzmán, F., et al. 2017, *RMxAA*, **53**, 385
 Fox, A. J., Cashman, F. H., Kriss, G. A., et al. 2023, *ApJL*, **946**, L48
 Fox, A. J., Frazer, E. M., Bland-Hawthorn, J., et al. 2020, *ApJ*, **897**, 23
 Fox, A. J., Lehner, N., Lockman, F. J., et al. 2016, *ApJL*, **816**, L11
 Fox, A. J., Wakker, B. P., Barger, K. A., et al. 2014, *ApJ*, **787**, 147
 Fox, A. J., Wakker, B. P., Savage, B. D., et al. 2005, *ApJ*, **630**, 332
 Gritton, J. A., Shelton, R. L., & Kwak, K. 2014, *ApJ*, **795**, 99
 Heald, G. H., Rand, R. J., Benjamin, R. A., & Bershadsky, M. A. 2007, *ApJ*, **663**, 933
 Heckman, T. M. 2002, in ASP Conf. Ser. 254, Extragalactic Gas at Low Redshift, ed. J. S. Mulchaey & J. T. Stocke (San Francisco, CA: ASP), 292
 Hopkins, P. F. 2015, *MNRAS*, **450**, 53
 Hopkins, P. F., Wetzel, A., Kereš, D., et al. 2018, *MNRAS*, **480**, 800
 Howk, J. C., Sembach, K. R., Savage, B. D., et al. 2002, *ApJ*, **569**, 214
 Jenkins, E. B. 1996, *ApJ*, **471**, 292
 Jenkins, E. B. 2009, *ApJ*, **700**, 1299
 Jenkins, E. B., & Wallerstein, G. 2017, *ApJ*, **838**, 85
 Kalberla, P. M. W., Burton, W. B., Hartmann, D., et al. 2005, *A&A*, **440**, 775
 Kalberla, P. M. W., McClure-Griffiths, N. M., Pisano, D. J., et al. 2010, *A&A*, **521**, A17
 Kallivayalil, N., van der Marel, R. P., Besla, G., Anderson, J., & Alcock, C. 2013, *ApJ*, **764**, 161
 Kamphuis, P., Peletier, R. F., Dettmar, R.-J., et al. 2007, *A&A*, **468**, 951
 Khaire, V., & Srianand, R. 2019, *MNRAS*, **484**, 4174
 Kim, S., Dopita, M. A., Staveley-Smith, L., & Bessell, M. S. 1999, *AJ*, **118**, 2797
 Kim, S., Staveley-Smith, L., Dopita, M. A., et al. 1998, *ApJ*, **503**, 674
 Kozłowski, S., Kochanek, C. S., Jacyszyn, A. M., et al. 2012, *ApJ*, **746**, 27
 Krishnarao, D., Fox, A. J., D’Onghia, E., et al. 2022, *Natur*, **609**, 915
 Krogager, J.-K. 2018, arXiv:1803.01187
 Kwak, K., Shelton, R. L., & Henley, D. B. 2015, *ApJ*, **812**, 111
 Lakićević, M., van Loon, J. T., Meixner, M., et al. 2015, *ApJ*, **799**, 50
 Leahy, D. A. 2017, *ApJ*, **837**, 36
 Lehner, N., & Howk, J. C. 2007, *MNRAS*, **377**, 687
 Lehner, N., Howk, J. C., Marasco, A., & Fraternali, F. 2022, *MNRAS*, **513**, 3228
 Lehner, N., Keenan, F. P., & Sembach, K. R. 2001, *MNRAS*, **323**, 904
 Lehner, N., Staveley-Smith, L., & Howk, J. C. 2009, *ApJ*, **702**, 940
 Lehner, N., Zech, W. F., Howk, J. C., & Savage, B. D. 2011, *ApJ*, **727**, 46
 Lopez, L. A., Krumholz, M. R., Bolatto, A. D., Prochaska, J. X., & Ramirez-Ruiz, E. 2011, *ApJ*, **731**, 91
 Lucchini, S., D’Onghia, E., & Fox, A. J. 2021, *ApJL*, **921**, L36
 Lucchini, S., D’Onghia, E., & Fox, A. J. 2024, *ApJ*, **967**, 16
 Lucchini, S., D’Onghia, E., Fox, A. J., et al. 2020, *Natur*, **585**, 203
 Maggi, P., Haberl, F., Kavanagh, P. J., et al. 2016, *A&A*, **585**, A162

- Mishra, S., Fox, A. J., Krishnarao, D., et al. 2024, *ApJL*, **976**, L28
- Nayak, O., Green, A., Hirschauer, A. S., et al. 2023, *ApJ*, **944**, 26
- Nidever, D. L., Majewski, S. R., & Burton, W. B. 2008, *ApJ*, **679**, 432
- Nomoto, K., Iwamoto, K., Nakasato, N., et al. 1997, *NuPhA*, **621**, 467
- Nomoto, K., Tominaga, N., Umeda, H., Kobayashi, C., & Maeda, K. 2006, *NuPhA*, **777**, 424
- Oosterloo, T., Fraternali, F., & Sancisi, R. 2007, *AJ*, **134**, 1019
- Oppenheimer, B. D., & Davé, R. 2008, *MNRAS*, **387**, 577
- Pellegrini, E. W., Oey, M. S., Winkler, P. F., et al. 2012, *ApJ*, **755**, 40
- Pingel, N. M., Dempsey, J., McClure-Griffiths, N. M., et al. 2022, *PASA*, **39**, e005
- Piskunov, N. E., Kupka, F., Ryabchikova, T. A., Weiss, W. W., & Jeffery, C. S. 1995, *A&AS*, **112**, 525
- Redman, M. P., Al-Mostafa, Z. A., Meaburn, J., & Bryce, M. 2003, *MNRAS*, **344**, 741
- Richter, P., de Boer, K. S., Werner, K., & Rauch, T. 2015, *A&A*, **584**, L6
- Richter, P., de Boer, K. S., Widmann, H., et al. 1999, *Natur*, **402**, 386
- Richter, P., Fox, A. J., Wakker, B. P., et al. 2013, *ApJ*, **772**, 111
- Roman-Duval, J. 2020, Hubble UV Legacy Library of Young Stars as Essential Standards (“ULLYSES”), STScI/MAST, doi:10.17909/T9-JZEH-XY14
- Roman-Duval, J., Jenkins, E. B., Tchernyshyov, K., et al. 2022, *ApJ*, **928**, 90
- Roman-Duval, J., Jenkins, E. B., Williams, B., et al. 2019, *ApJ*, **871**, 151
- Roman-Duval, J., Proffitt, C. R., Taylor, J. M., et al. 2020, *RNAAS*, **4**, 205
- Russell, S. C., & Dopita, M. A. 1992, *ApJ*, **384**, 508
- Savage, B. D., & de Boer, K. S. 1981, *ApJ*, **243**, 460
- Savage, B. D., & Sembach, K. R. 1991, *ApJ*, **379**, 245
- Savage, B. D., & Sembach, K. R. 1996, *ApJ*, **470**, 893
- Setton, D. J., Besla, G., Patel, E., et al. 2023, *ApJL*, **959**, L11
- Shelton, R. L., & Kwak, K. 2018, *ApJ*, **866**, 34
- Smith, R. C. & MCELS Team 1999, in IAU Symp. 190, New Views of the Magellanic Clouds, ed. H. Chu (Cambridge: Cambridge Univ. Press), 28
- Spitzer, L., Jr. 1996, *ApJL*, **458**, L29
- Springel, V. 2005, *MNRAS*, **364**, 1105
- Springel, V., & Hernquist, L. 2003, *MNRAS*, **339**, 289
- Staveley-Smith, L., Kim, S., Calabretta, M. R., Haynes, R. F., & Kesteven, M. J. 2003, *MNRAS*, **339**, 87
- Tepper-García, T. 2006, *MNRAS*, **369**, 2025
- van Loon, J. T., Bailey, M., Tatton, B. L., et al. 2013, *A&A*, **550**, A108
- Veilleux, S., Cecil, G., & Bland-Hawthorn, J. 2005, *ARA&A*, **43**, 769
- Viegas, S. M. 1995, *MNRAS*, **276**, 268
- Walborn, N. R. 1991, in IAU Symp. 148, The Magellanic Clouds, ed. R. Haynes & D. Milne (Dordrecht: Kluwer), 145
- Werk, J. K., Rubin, K. H. R., Bish, H. V., et al. 2019, *ApJ*, **887**, 89
- Wiersma, R. P. C., Schaye, J., & Smith, B. D. 2009, *MNRAS*, **393**, 99
- Zheng, Y., Tchernyshyov, K., Olsen, K., et al. 2024, *ApJ*, **974**, 22